Ciliary transition zone proteins coordinate ciliary protein composition and ectosome shedding

Liang Wang
Jiangsu Normal University https://orcid.org/0000-0001-5950-0593
Xin Wen
Jiangsu Normal University
Zhengmao Wang
Tsinghua University
Zaisheng Lin
Shanghai Jiao Tong University
Chunhong Li
Jiangsu Normal University
Huilin Zhou
Jiangsu Normal University
Huimin Yu
Jiangsu Normal University
Yuhan Li
Jiangsu Normal University
Yifei Cheng
Jiangsu Normal University
Geer Lou
Shanghai Biotree Biotech Co. Ltd
Junmin Pan
Tsinghua University https://orcid.org/0000-0003-1242-3791
Muqing Cao (muqingcao@sjtu.edu.cn)
Shanghai Jiao Tong University https://orcid.org/0000-0002-0352-6548

Article

Keywords: cilia, transition zone, TCTN1, ectosome

Posted Date: December 8th, 2021

DOI: https://doi.org/10.21203/rs.3.rs-1142196/v1

Version of Record: A version of this preprint was published at Nature Communications on July 9th, 2022.
See the published version at https://doi.org/10.1038/s41467-022-31751-0.

Ciliary transition zone proteins coordinate ciliary protein composition and ectosome shedding

Liang Wang[1, #, *], Xin Wen[1, #], Zhengmao Wang[2], Zaisheng Lin[3], Chunhong Li[1], Huilin Zhou[1], Huimin Yu[1], Yuhan Li[1], Yifei Cheng[1], Geer Lou[4], Junmin Pan[2], Muqing Cao[3, *]

[1]School of Life Sciences, Jiangsu Normal University, Xuzhou 221116, China

[2]School of Life Sciences, Tsinghua University, Beijing 100084, China; Laboratory for Marine Biology and Biotechnology, Qingdao National Laboratory for Marine Science and Technology, Qingdao 266071, China

[3]Key Laboratory of Cell Differentiation and Apoptosis of Chinese Ministry of Education, Department of Pathophysiology, Shanghai Jiao Tong University School of Medicine, Shanghai 200025, China

[4]Shanghai Biotree Biotech Co. Ltd, Shanghai 201815, China

[#]L.W., and X.W. contributed equally to this work.

[*]To whom correspondence may be addressed. **Email:** wangliang@jsnu.edu.cn, muqingcao@sjtu.edu.cn.

Lead contact: L.W. **Email:** wangliang@jsnu.edu.cn.

Keywords: cilia; transition zone; TCTN1; ectosome

This PDF file includes:

Manuscript Text
Figures 1 to 7
Supplementary Figures 1 to 6

Abstract

The transition zone (TZ) of the cilium/flagellum serves as a diffusion barrier that controls the entry/exit of ciliary proteins. Mutations of the TZ proteins disrupt barrier function and lead to multiple human diseases. However, the systematic regulation of ciliary composition and signaling-related processes by different TZ proteins is not completely understood. Here, we reveal that loss of TCTN1 in *Chlamydomonas reinhardtii* disrupts the assembly of Y-links in the TZ. Proteomic analysis of cilia from WT and three TZ mutants, *tctn1*, *cep290*, and *nphp4*, showed a unique role of each TZ subunit in the regulation of ciliary composition, explaining the phenotypic diversity of different TZ mutants. Interestingly, we found that defects in the TZ impair the formation and biological activity of ciliary ectosomes. Collectively, our findings provide systematic insights into the regulation of ciliary composition by TZ proteins and reveal a link between the TZ and ciliary ectosomes.

Main Text

Introduction

Cilia and flagella, conserved antenna-like structures protruding from cell surfaces, harbor a number of signaling-associated molecules that maintain cellular homeostasis and regulate tissue development [1, 2, 3]. To control the specific ciliary composition, a specialized zone at the base of cilia named the transition zone (TZ) serves as a gatekeeper to sort proteins into/out of the cilia [4, 5, 6]. Defects in TZ genes cause a variety of syndromes, termed ciliopathies, including Meckel–Gruber syndrome (MKS), nephronophthisis (NPHP), Joubert syndrome (JBTS), Senior-Loken syndrome (SLSN), and oral-facial-digital (OFD) syndrome, characterized by polydactyly, kidney cysts, ataxia, hyperpnea, nervous system degeneration, and developmental delay [7, 8, 9, 10, 11, 12]. The function of the TZ structure relies on the integrity of two major complexes located at the TZ region, termed the MKS complex and NPHP complex, including MKS1, TMEM67, TMEM216, B9D1, B9D2, CEP290, and TCTN1-3 for the MKS complex and NPHP1, NPHP4, NPHP8, and NPHP2 for the NPHP complex [9, 13]. Defects in any gene encoding a protein in the two complexes have been associated with various human diseases, indicating the indispensable function and different role of each member. To date, how each TZ protein uniquely and systematically controls the sorting of ciliary proteins for ciliary assembly and signaling remains largely unknown.

Ectosomes, vesicles secreted from the cell surface, are composed of various types of proteins and RNAs and mediate cellular communication in cell populations [14, 15, 16, 17, 18]. Surprisingly, the ciliary membrane is capable of generating ectosomes, and the shedding of ciliary ectosomes plays multiple roles in biological processes [19, 20, 21, 22, 23, 24, 25]. Unlike mammalian cells shedding off both ectosomes and exosomes from plasma membrane with distinct assembly mechanisms and diameters, cilia are the unique source of ectosomes derived from *C. reinhardtii* cells surrounded by cell walls, making *C. reinhardtii* as an ideal model for the study on the mechanism of ectosomes shedding [17, 19, 20]. However, whether the TZ, a major regulator of ciliary components and signaling, has functions in the release of ciliary ectosomes is a potentially interesting and important area of investigation.

In this study, we identified a mutant cell line of *C. reinhardtii.* The disrupted gene encodes a homolog of mammalian TCTN proteins; thus, we named the mutant *tctn1*. Our results showed that *C. reinhardtii* TCTN1 localized to the TZ

region independent of CEP290 and NPHP4, and the loss of TCTN1 largely attenuated the formation of Y-links in the TZ. Taking advantage of cilia isolation in *C. reinhardtii*, we purified cilia from WT and three TZ mutants, *tctn1*, *nphp4*, and *cep290*. Proteomic analysis of the cilia indicated that each gate molecule played a unique role in the control of ciliary proteins into/out of cilia, although some common functions were observed. Furthermore, we found that disruption of the TZ altered the size and biological activities of ciliary ectosomes. Systematic proteomics profiling and ectosome analysis showed that each TZ protein has a unique function in ciliary events, including ciliary protein sorting and ciliary ectosome shedding.

Results

Loss of TCTN1 attenuates ciliogenesis in *C. reinhardtii*

To identify new genes involved in ciliary assembly, we performed an unbiased forward genetic screen in a mutant library generated by insertional mutagenesis and found one cilia-deficient cell line. Restriction enzyme site-directed PCR (RESDA-PCR) showed that the insertion was located in the fifth exon of the *Cre03.g181450* gene (Fig. 1a), which encodes a 679 aa homologous protein of mammalian TCTN1, 2, and 3 (Fig. 1b). Since there is only one TCTN homolog in *C. reinhardtii*, we named the mutant *tctn1*. In contrast to wild-type cells with two equal-length cilia, *tctn1* cells were palmelloid without visible cilia (Fig. 1c, d), indicating fail of lysis of mother cell wall after mitosis. Transformation of the *tctn1* mutant with an HA-tagged full-length *TCTN1* DNA fragment restored *TCTN1* expression (Supplementary Fig. 1a) and rescued the defect in ciliary assembly (Fig. 1c and Supplementary Fig. 1b), which confirmed that the ciliary phenotype was caused by the mutation in *TCTN1*. Autolysin, the proteolytic enzyme, is often used for lysis of cell wall to hatch daughter cells [19, 26]. Upon autolysin enzyme treatment, *tctn1* cells hatched from the mother cell wall and assembled cilia (Fig. 1e). However, the average final ciliary length after hatching reached ~ 8 μm, which was shorter than that of WT cells (Fig. 1f, g), and occasionally bulges at the tip of short cilia were observed (Fig. 1e). It was reported that the TZ functioned in deciliation, ciliary assembly, and disassembly in other organisms [27, 28, 29], so we determined the excision, regeneration and resorption of the cilia in the *tctn1* cells. Consistent with the WT and rescued cells, *tctn1* cells showed no defects in the deciliation process and completed the ciliary regeneration to reach the original length 2 hours after deciliation by pH shock, but the mutants showed slower ciliary assembly kinetics (Fig. 1g). Interestingly, in the cilia shortening process induced by Nappi, *tctn1* cells showed faster ciliary disassembly kinetics (Fig. 1h).

TCTN1, 2, and 3 localize at the TZ in other model organisms [30, 31]. Immunostaining analysis of the rescued cell line expressing TCTN1-HA showed that TCTN1 in *C. reinhardtii* is also a TZ protein at the base of the cilium (Fig. 1i). Consistently, polyclonal antibodies against endogenous *C. reinhardtii* TCTN1 showed the same TZ staining pattern in the WT and rescued lines but not in the *tctn1* mutant (Supplementary Fig. 1c). The polyclonal antibodies against endogenous TCTN1 showed additional signal in the cell body compared with the HA antibody (Fig. 1i and Supplementary Fig. 1c). Because the antibodies against the endogenous TCTN1 showed signals in cell bodies of the *tctn1* cells, which lost TCTN1 protein, it was very possible that the staining of the cell body was nonspecific. Consistent with previous studies for other TZ protein, TCTN1 was also associated with the ciliary base after deciliation and reciliation (Supplementary Fig. 1d) [32, 33]. Immunoblot analysis of whole cells, cell bodies, and cilia verified that TCTN1 was not present in cilia (Fig. 1j), which is consistent with proteomic studies of cilia and the TZ

in *C. reinhardtii* [34, 35]. Taken together, these data demonstrated that *C. reinhardtii* TCTN1 is a TZ protein and functions in ciliogenesis.

Loss of TCTN1 causes ultrastructural defects in the TZ

C. reinhardtii is an ideal model for transmission electron microscopy (TEM) studies of the ultrastructure of cilia, especially the TZ. TEM revealed that the bulges in the short cilia were filled with electron-dense material (Fig. 2a). The elongated cilia of *tctn1* mutant cells showed a normal ultrastructure with 9+2 microtubule doublets (Supplementary Fig. 2a). In the longitudinal sections through the TZ, Y-links (also called wedge-shaped structures or Y-linkers) were present in WT and rescued cells but were missing in *tctn1* cells (Fig. 2b). In the cross sections, the Y-links bridging the TZ microtubules and ciliary membrane were often absent in *tctn1* cells (Fig. 2c). Disruption of Y-links impairs the connection between the microtubule axoneme and the ciliary membrane [33]. We measured the distance between the H structure and the ciliary membrane in WT, *tctn1* and rescued cells and found that the distance was greater in *tctn1* mutant cells than in WT or rescued cells (Fig. 2d).

Localization of TCTN1 in the TZ is independent of CEP290 or NPHP4

To further illustrate the localization of TCTN1, we performed immunostaining with antibodies against HA, acetylated α-tubulin, and CEP290 or NPHP4 and found that TCTN1 was distal to CEP290 but proximal to NPHP4 (Fig. 2e, f). Furthermore, we carried out immunostaining assays in *tctn1*, *cep290*, *nphp4*, and WT cells and found that the localization of TCTN1, CEP290, and NPHP4 was independent of the other two proteins (Fig. 2g).

The ciliary phenotypes of *tctn1*, *cep290*, and *nphp4* are variable

The integrity of the TZ affects ciliary morphology and motility. *cep290* are often palmelloid and immotile, while *nphp4* have normal cilia with slightly defective swimming linearity [33, 36]. We compared the phenotypes of *tctn1*, *cep290*, and *nphp4*. The *tctn1* cells were palmelloid and immotile in TAP medium, similar to *cep290* (Supplementary Fig. 2b). After autolysin treatment, *tctn1* cells were released from the mother cell wall, and the cilia were gradually assembled. Approximately 90% of *tctn1* cells had cilia 3 hours after autolysin treatment, and the final average ciliary length was 7.94 ± 1.14 μm (Supplementary Fig. 2b, c). For *cep290*, ~ 54% of cells had cilia with a final average length of 9.47 ± 0.54 μm (Supplementary Fig. 2b, c). Occasionally, we found that when the mutant *tctn1* cells were cultured in M medium (minimal media) at low cell density, the *tctn1* cells were not palmelloid, and ~ 66% of cells had cilia (8.81 ± 0.75 μm) and swam normally, while this phenotype was not found in *cep290* (Supplementary Fig. 2b). Compared to WT cells (ciliary length, 11.42 ± 0.94 μm) and *nphp4* cells (ciliary length, 11.60 ± 0.98 μm), *tctn1* and *cep290* cells were paralyzed. Consistently, more ciliary bulges were observed in *tctn1* and *cep290* cells (Supplementary Fig. 2d). In addition, *tctn1* and *cep290* cells showed slower ciliary regeneration kinetics than WT and *nphp4* cells (Supplementary Fig. 2e). Therefore, these collective data suggest that TCTN1 and CEP290 might play more essential roles in organization of the TZ and sorting of ciliary proteins than NPHP4.

The DUF1619 domain is essential for the function of TCTN1

DUF1619 (PF07773, IPR011677) is the only conserved domain identified in the TCTN protein family, but the function of this domain is not clear. To determine the function of DUF1619 for TCTN1, we constructed the truncated

mutants, TCTN1 (DUF1619) and TCTN1 (△DUF1619) (Fig. 3a). Through transformation of *tctn1* cells with the indicated HA-tagged mutants, we generated cell lines with deletion variants (Fig. 3a, b). Transformants were screened for the expression of truncated versions of TCTN1 by immunoblotting (Fig, 3b). The transformants with correct expression were used for the following experiments. Phenotypic analysis showed that two of the deletion mutant transformants examined were palmelloid, which phenocopied the *tctn1* mutant (Fig. 3c). Additionally, the ciliary bulges, motility, ciliary length, and ciliary assembly kinetics of the two transformants were comparable to those of *tctn1* cells (Fig. 3d and Supplementary Fig. 3a-c). These data demonstrate that the DUF domain is critical for TCTN1 function.

Loss of *TCTN1* systematically disrupts ciliary components

It has been reported that TCTN proteins contribute to the concentration of several ciliary membrane proteins in mammalian cells and worms [31, 37, 38]. However, the systematic changes in the ciliary protein composition in TZ mutants are unknown. The cilia of WT and *tctn1* were isolated and subjected to silver gel staining and proteomic analysis. Total ciliary protein (Cilia) and the membrane-matrix (M+M) and axonemal (Axo) fractions from the WT, *tctn1* and/or rescued cells were analyzed via SDS–PAGE. Significant differences between the WT and *tctn1* cilia were identified (Fig. 4a). To profile the systematic changes in ciliary proteins, we performed proteomic analysis of WT and *tctn1* cilia. Unexpectedly, a volcano plot showed that more proteins in cilia were increased in *tctn1* (Fig. 4b), which indicates that defects in the TZ not only impaired ciliary membrane protein concentration but also led to loss of the filter function to exclude other proteins (Fig. 4c). Clearly, the histogram showed an increase in IFT complexes, IFT motors, Golgi, chloroplast and mitochondrion proteins in cilia (Fig. 4c). Immunofluorescence and immunoblot analyses confirmed our proteomic data (Fig. 4d, e and Supplementary Fig. 4a, b). Surprisingly, the organelle proteins that presumably are not normally present in cilia but reside in the Golgi, chloroplast, and mitochondrion were transported into the cilia of the *tctn1* mutant (Fig. 4c). We verified these data via immunofluorescence and immunoblotting assays with antibodies against PSBC and PSAD (Fig. 4f, g). Immunofluorescence with anti-PSBC and anti-PSAD antibodies showed cup-shaped chloroplasts in cell bodies (Supplementary Fig. 5a, b) and abnormal accumulation of PSBC and PSAD in the cilia of *tctn1* cells (Fig. 4g). Collectively, the above results indicate that the defective TZ permitted entry of cytoplasmic proteins into cilia, which was consistent with the presumed function of the TZ in excluding nonciliary proteins and the gating roles of ciliary proteins in cilia.

Different TZ proteins regulate the specific protein composition of cilia

The phenotypic differences of the TZ mutants suggest that each TZ protein plays specific roles in control of ciliary composition. To systematically assess the functions of the TZ proteins in ciliary composition regulation, we performed proteomic analysis of cilia purified from WT, *tctn1*, *cep290*, and *nphp4* cells. In total, 2845 proteins were identified, and their relative abundances were determined. A heatmap indicated that the protein profile of each mutant cell was significantly unique (Supplementary Fig. 6a). Although the heatmap pattern of *nphp4* ciliary proteins was similar to that of the WT cilia, ~ 30.9% of the proteins showed threefold changes (>3 or <1/3) compared to the WT cilia (Supplementary Fig. 6a). Mutations in *TCTN1* or *CEP290* seemed to cause more severe defects in the TZ, which led to 51.8% or 60.9% of proteins showing threefold changes, respectively (Supplementary Fig. 6a).

Furthermore, according to the protein function, we performed grouped comparisons with WT and TZ mutants (Fig. 5a-d). Cargo transport-related proteins, including IFT/motor/BBS proteins, accumulated in the cilia of *tctn1* and *cep290* (Fig. 5a), while ciliary structural proteins, such as axonemal components, were downregulated in the cilia of *tctn1* and *cep290* (Fig. 5b). The regulation of ciliary membrane proteins seemed to be completely disrupted in the cilia of TZ mutants (Fig. 5c). Consistent with the proteomic results for *tctn1*, the nonciliary proteins from the Golgi, chloroplast, and mitochondrion were mistransported into the cilia of *cep290* mutants (Fig. 5d). The amount of ciliary membrane proteins, IFT proteins, and axonemal proteins was confirmed by immunoblot analysis (Supplementary Fig. 6b). Through immunofluorescence, we also verified that the chloroplast proteins of PSBC and PSAD were mislocated in the cilia of *cep290* and *tctn1* cells (Fig. 5e-g). These results demonstrate that loss of each TZ protein leads to unique and systematic changes in ciliary composition, which account for specific disruptions in ciliary signaling.

TZ proteins regulate the formation of ciliary ectosome during gamete mating

Cilia-derived ectosomes contain biologically active molecules and have multiple functions in the regulation of ciliary signaling [19, 21, 23, 24, 39, 40]. From the ciliary proteomics data, we noticed that the amount of ectosome-related proteins was disrupted in the cilia of mutant cells (e.g., FOX1, AGG3, FEA2, AGG4, FAP212, CYN20-1) (Fig. 6a) [20]. Considering the essential role of the TZ in ciliary membrane composition control, it is possible that ciliary ectosome formation may be affected by defects in the TZ. Additionally, defects of the TZ mutant in hatching from the mother cell wall also suggested alteration of ectosome formation in the TZ mutant cilia.

In the mating process, gametic cells release large amounts of ectosomes that activate other gametes by binding to the cilia of cells with opposite mating types [22, 25]. We mixed gametic cells (21*gr* × 6145c [WT]; *tctn1* × 6145c [*tctn1*]; *cep290* × 6145c [*cep290*]; *nphp4* × 6145c [*nphp4*]) at a ratio of 5:1, in which ectosomes from plus gametes constituted the majority. We purified ciliary ectosomes, followed by the negative staining TEM to visualize the morphology of ciliary ectosomes. Images revealed that the diameters of the ectosomes in the TZ mutant groups were significantly smaller than those in the control group (Fig. 6b, c). The average diameter of ectosomes from WT was 198.20 ± 4.66 nm (n=500), while the diameters of the ectosomes from *tctn1*, *cep290*, and *nphp4* were 87.35 ± 1.98 nm (n=500), 83.99 ± 1.72 nm (n=500), and 134.40 ± 3.93 nm (n=500), respectively (Fig. 6c). Moreover, the size distribution varied greatly among these ectosomes. For *tctn1* and *cep290*, the diameter of most ectosomes was 50–100 nm, while the diameter of most ectosomes of *nphp4* was slightly larger, with a distribution range of 50–100 nm and 100–150 nm (Fig. 6d). These data indicate that the TZ structure plays a role in the formation of ciliary ectosomes.

Ciliary ectosomes from the TZ mutants showed different biological activity and protein composition

Our previous studies showed that ciliary ectosomes exhibit biological activity to induce gamete agglutination of single mating type gametes and activate cilium-generated signaling during the mating process [22]. This behavior of single mating type gametes agglutination induced by the ciliary ectosomes is very similar to the bona fide mating agglutination, thus we name this behavior as pseudomating. Hence, the pseudomating is a possible assay to evaluate the bioactivity of the ciliary ectosomes. Thus, another interesting question is whether the activities of the ectosomes from the TZ mutants were altered. To avoid possible contamination with cell debris that may be pelleted

during ultracentrifugation, we performed ectosome purification using a commercial exosome/ectosome isolation kit, which specifically precipitated the membrane vesicles upon relatively low-speed centrifugation (at 10,000 × *g*). As denoted in Material and Methods, we conducted a gamete pseudomating assay with the fractions of S20, Sup and Eco, and found that the purified ectosomes, but not the supernatant fraction, possessed the ability to induce the adherence of 6145c gametic cells, not 6145c vegetative cells or 6145c gametic cells alone (Fig. 7a, b). After mixing with the ectosomes for 10 minutes, we measured the percentages of the adhering minus gametes (6145c) and found that the efficiency of the ectosomes from the TZ mutants, especially from the *tctn1* or *cep290* group, decreased dramatically (Fig. 7c). Consistent with Fig. 7*B*, the ectosomes failed to induce agglutination of vegetative 6145c cells in Con group (Fig. 7c). As expected, SDS–PAGE with silver staining showed variations in the protein composition and amount of ectosomes from the four groups (Fig. 7d). Thus, these data further demonstrate that the TZ also plays roles in regulation of the biological activity and protein composition of ciliary ectosomes.

Discussion

As the only transport route from the cell body to the cilium, the TZ compartment plays essential roles in the regulation of ciliary composition, which fundamentally defines the biological processes and functions of the cilium. Although the structure and composition of the TZ have been characterized, the unique roles of TZ proteins in assembly of the TZ and their systematic regulation of ciliary components are largely unknown. Consistent with previous studies in mammals and worms [9, 30, 35, 41, 42, 43, 44, 45, 46], we found that *C. reinhardtii* TCTN1 localizes in the TZ (Fig. 1i, j). Furthermore, we provide both ultrastructural insights and systematic proteomic information upon the loss of TCTN1. Using immunofluorescence microscopy, we showed that TCTN1 localized in the middle region of the TZ independent of CEP290 and NPHP4 (Fig. 2e, f). Using TEM, we found that TCTN1 is essential for assembly of the Y-links in the TZ, similar to CEP290 (Fig. 2b-d) [33]. Previous studies indicated that TCTN1 is located at the ciliary membrane and CEP290 is located near the axoneme [47]. Based on our data, we speculate that TCTN1 and CEP290 may function as anchors of the Y-links at the two ends, and loss of either of the two key components thoroughly disrupts the structure.

The TZ strictly regulates the entry and retention of ciliary proteins and exclusion of nonciliary proteins [9, 33, 43, 48, 49]. It is known that the severity of TZ defects caused by mutations in individual TZ proteins varies, reflecting the different functions of individual proteins in organizing the TZ. Consistently, our phenotypic analysis of the three TZ mutants (*tctn1*, *cep290*, and *nphp4*) also showed various ciliary phenotypes (Supplementary Fig. 2b-e), which were caused by the different systematic changes in the ciliary components (Supplementary Fig. 6a). To date, how the loss of a single TZ protein systematically affects ciliary composition is not clear. Taking advantage of cilia purification from *Chlamydomonas*, we isolated the cilia of WT, *tctn1*, *cep290*, and *nphp4* cells and subjected the ciliary samples to proteomic analysis. In agreement with the variable phenotypes, the proteomic profile of cilia from each cell type was quite unique (Fig. 5a-d and Supplementary Fig. 6a). The concentrations of ciliary membrane-associated proteins, including PKD, FOX1, AGG4, and CYN20-1, were disrupted in *tctn1*, *cep290*, and *nphp4* mutant cilia. Considering the function of membrane proteins, ciliary signaling should be misregulated. Although mutants displayed characteristic protein profiles and the protein ratios were variable in different mutants, we indeed observed several common features shared by the three TZ mutants. First, the proteomic data showed accumulation of IFT subunits and several IFT motors and reduction of the axonemal components in the mutant cilia. Second, nonciliary proteins,

including various ATP synthases (ATP1A, ATP2, ATPC, and ASA4), photosystem proteins (PSAD, PABC, PSAA, and PSAB), vesicular transport proteins (Coatomer subunits), and translation initiation factors (EIF3 subunits), also accumulated to different degrees, which is direct evidence of the function of the TZ to exclude nonciliary components. However, thus far, we do not know how these nonciliary proteins could pass through the ciliary gate and whether they have functions in cilia. Furthermore, according to the above phenotypic analysis and ciliary protein profiling in these three TZ mutants (*tctn1*, *cep290*, *nphp4*), we conclude that the different roles of TCTN1, CEP290 and NPHP4 in protein sorting ultimately influence the phenotype. The hierarchy of degrees of phenotypic severity in the three TZ genes is *CEP290* > *TCTN1* > *NPHP4*. How they coordinately influence ciliary composition and ciliary functions remains to be further investigated.

Another interesting phenomenon observed in our data inspire us that there may be a link between the TZ proteins and ciliary ectosomes. First, the cellular morphology of TZ mutants (*tctn1* and *cep290*) are palmelloid (Fig. 1c and Supplementary Fig. 2b) [33], indicating the deficient of ciliary ectosome associated lysis protease shedding within the mother cell walls after cell division [19]. Second, the proteomic analysis was changes in ciliary ectosome-associated proteins (e.g., FOX1, AGG4, CYN20-1) (Fig. 6a) [20]. Until now, it has been unknown whether the TZ structure controls the formation of ciliary ectosomes. Here, we provide direct evidence that defines the function of the TZ in ectosome biogenesis. Loss of the integrity of the TZ affects the morphology, protein composition, and biological activities of ciliary ectosomes (Fig. 6 and Fig. 7). In the future, it will be worth investigating the mechanisms through which TZ proteins influence the amount of ectosome-associated proteins in cilia and the control of ectosome formation and biological activity.

In summary, our work showed that TCTN1 is essential for proper assembly of the Y-links of the TZ. Using proteomic analysis of cilia from WT, *tctn1*, *cep290*, and *nphp4* cells, we systematically characterized the ciliary protein profile of the mutants, which revealed the unique function of each TZ protein. Most importantly, a novel function of the TZ in ciliary ectosome formation was uncovered.

Methods

Strains and cell culture

C. reinhardtii wild-type strains 21*gr* (CC-1690, wild-type, mt+) and 6145c (CC-2895, wild-type, mt-) and the mutant strains *cep290* (CC-4374, mt+) and *nphp4* (CC-5113, mt+) were provided by the *Chlamydomonas* Resource Center (University of Minnesota, USA). The *tctn1* mutant was generated from the wild-type strain 21*gr* by insertional mutagenesis with the paromomycin-resistant DNA fragment *aphVIII*. Strains were cultured in Tris-acetate-phosphate (TAP) plates or liquid medium with aeration at 23 ± 0.5 °C with a light/dark cycle of 14/10 h at a light intensity of 8000 lx. For transformation experiments, the indicated cell line was grown in TAP liquid medium under continuous light. Autolysin was used to release *tctn1* and *cep290* mutant cells from the mother cell wall and to induce ciliogenesis. For the induction of gametogenesis, vegetatively growing cells were transferred to N-free medium as previously described [22]. For *tctn1* or *cep290* gametes, autolysin was applied to induce the release of gametes from the palmelloid before mating. The cells were thoroughly washed to remove autolysin and allowed to assemble cilia for ~ 2 h.

DNA manipulations, transformation, and mutagenesis

A library of mutants was generated via random insertional using electroporation with the *aphVIII* gene (paromomycin-resistant cassette, ~ 2.1 kb fragment cut with *EcoRI* from the plasmid pJMG-aphVIII) [50]. Electroporation was performed as described previously [50]. Briefly, cells for transformation were cultured in liquid TAP medium with constant aeration and continuous light until the cell concentration reached ~ 1.0 × 10^7 cells/mL. Then, the cells were inoculated into fresh liquid TAP medium and grown under continuous light for 18–20 h until the cell concentration reached ~ 4.0 × 10^6 cells/mL. Cells were transformed with the DNA fragment via square-wave electroporation with a BTX ECM830 electroporation apparatus (500 V, 4 ms, 6 pulses) (BTX, USA). The flanking sequences of the *aphVIII* insertional site were determined by restriction enzyme site-directed PCR (RESDA-PCR) [51], sequencing and blasting with *Chlamydomonas reinhardtii* v5.5 genome database (https://phytozome.jgi.doe.gov/pz/portal.html#). For the gene complementation experiments, full-length DNA harboring the *TCTN1* locus (with an endogenous promoter) was inserted into the expression construct pHyg-3HA. For construction of deletion mutants of the *TCTN1* gene, all deletion mutant constructs were generated based on the wild-type *TCTN1* construct and are indicated in the text. The resulting constructs were then linearized with *NdeI* (Takara, Japan) and transformed into *tctn1* mutant with electroporation. The transformants were plated onto the hygromycin (Sigma, USA) plates and screened for the ciliary phenotypes and via immunoblot analysis.

Analysis of ciliary and cellular phenotypes

The liquid-medium-cultured cells were put on the slide, and observed the cell status with inverted microscope. To capture the cell images, cells were fixed with 5% glutaraldehyde solution, plated on the slide with a cover-slip, observed and captured by LAS V4.0 imaging software on a Leica DMI4000 B Inverted Microscope (Leica, Germany) with a 10 ×, 20 ×, 40 × or 63 × objective (HCX PL FLUOTAR 10 × / 0.30, 506507; HCX PL FLUOTAR L 20 × / 0.40, 506243; HCX PL FLUOTAR L 40 × / 0.60, 506203; HCX PL FLUOTAR L 63 × / 0.70, 506217) for differential interference contrast (DIC)/ phase contrast (PH) images. The ciliary length was measured for 50 cells by ImageJ (National Institutes of Health, USA). The cell number was counted for 200 cells. All original data were analyzed and plotted with GraphPad Prism (GraphPad Software, USA). All experiments were repeated three times.

Ciliary deciliation, regeneration, and resorption

To induce the ciliary deciliation, cells was deciliated by pH shock method [52, 53]. Briefly, cells were quickly treated with 0.5 M glacial acetic acid, kept at pH ~ 4.5 for 30 s, then quickly added by 0.5 M KOH to recover the pH ~ 7.0. To induce regeneration of the cilia, cells after deciliation were centrifuged and washed with fresh M medium to be allowed for ciliary regeneration with aeration at 23 ± 0.5 °C in light. To induce resorption of the cilia, cells incubated with 20 mM sodium pyrophosphate (NaPPi) in M medium gradually shorten cilia over time [54]. At the indicated time point, cells were collected for imaging and measurement of ciliary length or for the immunoblot analysis. All experiments were repeated three times.

Autolysin preparation

The cell wall proteolytic enzyme autolysin is typically generated during plus and minus gametes mating [26]. Generally, we followed the gamete autolysin preparation procedure (https://www.chlamycollection.org/methods/preparation-of-gamete-autolysin/), except M-N medium for nitrogen starvation was used to induce gamete differentiation. Then cells at the density of ~ 3.0 × 10^6 cells/mL were incubated in M-N medium for 20 ~ 24 h under continuous light (8000

lx). Equal amount of opposite mating type gametes (21*gr* × 6145c) were mixed to allow mating with gentle aeration for ~ 15 min. After centrifugation at 600 × *g*, for 5 min and 14, 000 × *g*, for 10 min respectively, the final supernatant was filtrated by 0.22 μm membrane filter and aliquot, stored at – 80 °C until use.

Isolation and fractionation of cilia and ciliary ectosomes

To isolate cilia, cells were deciliated by pH shock. Detached cilia were enriched via sucrose gradient centrifugation and pelleted by high-speed centrifugation [55]. To fractionate the ciliary samples into the M+M (membrane and matrix) fraction and Axo (axoneme) fraction, the ciliary pellet was lysed in 0.5% NP40 buffer A (50 mM Tris-HCl [pH 7.5], 10 mM $MgCl_2$, 1 mM EDTA, 1 mM DTT) with EDTA-free protease inhibitor cocktail (Roche, Switzerland), frozen in liquid nitrogen and thawed, followed by centrifugation at 20,000 × *g* at 4 °C for 10 min. The supernatants and pellets were the M+M fraction and Axo fraction, respectively.

Isolation of ciliary ectosomes by ultracentrifugation was carried out as described previously [22] with slight modifications. Briefly, The mating type plus (mt+) gametes (21*gr*, *tctn1*, *cep290*, and *nphp4*) are mixed with the mating type minus (mt-) gametes 6145c (mt+: mt- =5: 1) for 15 min, followed by 600 × *g* for 5 min, 20, 000 × *g* for 10 min, and the final step of 150, 000 × *g*, 60 min to obtain the ectosome pellet (Eco). The ciliary ectosomes were also purified with a Total Exosome Isolation (from cell culture media) Kit (Cat. No. 4478359, ThermoFisher, USA). The media with above described mating cells were centrifuged at 600 × *g* for 5 min and 20,000 × *g* for 5 min (3 times) to remove the cells and debris. The resulting supernatant (S20) was finally incubated in buffer at 4 °C for 2 h and then pelleted by centrifugation at 10,000 × *g* for 60 min to obtain the final supernatant (Sup) and ectosome pellet (Eco). The pelleted ectosomes were resuspended in N-free medium. The ectosomes were image by TEM. At least 500 ectosomes were measured for their diameters by ImageJ software for each group. The experiments were performed for three times.

Assay for ectosome activity

To determine the activity of ectosomes, purified ectosomes were applied for gamete agglutination with 6145c. In particular, ectosomes from different mating events (21*gr*, *tctn1*, *cep290*, or *nphp4* × 6145c) were mixed with 6145c gametes (10 μL, 1.0 × 10^8 cells/mL) to induce agglutination for 10 min. The agglutinating gametes were observed and imaged alive. The ratios of cell adhesion were plotted using GraphPad Prism software (GraphPad Software, USA).

Immunofluorescence microscopy

Immunofluorescence was carried out essentially as previously described [52]. For detection of CEP290 and NPHP4, cells were collected and resuspended in MT buffer (30 mM HEPES [pH 7.2], 3 mM EGTA, 1 mM $MgSO_4$, 25 mM KCl), followed by fixation and extraction in 100% prechilled methanol for 20 min at -20 °C. For detection of other proteins, cells were collected and resuspended in MT buffer for 2 min, followed by fixation in 4% paraformaldehyde fixation solution (Biosharp, China) for 5 min at room temperature. After the fixation step, cells were resuspended in MT buffer with 0.5% NP-40 for 2 min and further extracted in 100% prechilled methanol for 10–15 min at -20 °C. The cells were then sequentially rehydrated with PBS, blocked with goat blocking buffer (containing 5% goat serum) (Sangon Biotech, China), and incubated with primary antibodies at 4 °C overnight, followed by incubation with secondary antibodies at 37 °C for 2 h.

The secondary antibodies used were preadsorbed anti-rat IgG H&L (Alexa Fluor® 488), preadsorbed anti-mouse IgG H&L (Alexa Fluor® 594), preadsorbed anti-rabbit IgG H&L (Alexa Fluor® 647), preadsorbed anti-rabbit IgG H&L (Alexa Fluor® 594), preadsorbed anti-rabbit IgG H&L (Alexa Fluor® 488), and preadsorbed anti-mouse IgG H&L (Alexa Fluor® 647) (Abcam, UK). The secondary antibodies were used at a dilution of 1:500.

After three washes for 5 min with 0.5% Tween-20 PBS, one wash with PBS, and one wash with Milli-Q, samples on the slides were mounted with DAPI-Fluoromount-G (SouthernBiotech, USA), sealed with nail polish and air dried for ~ 2 h before observation. Samples were then imaged on a Leica TCS SP5-II or Leica TCS SP8 confocal laser microscope (Leica, Germany) with a 63 × oil immersion objective (HCX PL APO 63 × / 1.40–0.60 OIL CS, 506188). Images were acquired and processed using Leica Application Suite AF or Leica Application Suite X and Adobe Photoshop and assembled using Adobe Illustrator (Adobe Systems Incorporated, USA).

SDS–PAGE and immunoblotting

Cells were harvested by centrifugation at 10,000 × *g* for 1 min, frozen in liquid nitrogen and stored at -80 °C until use. The frozen samples were then lysed in prechilled buffer A (50 mM Tris-HCl [pH 7.5], 10 mM $MgCl_2$, 1 mM EDTA, 1 mM DTT) with EDTA-free protease inhibitor cocktail (Roche, Switzerland) and boiled in 1 × SDS sample buffer for 5 min before being subjected to SDS–PAGE and blotting analysis. The secondary antibodies used were HRP-conjugated goat anti-mouse, goat anti-rabbit and goat anti-rat (1:5000; Jackson, USA). The final immunoreactive bands were visualized and analyzed using an Amersham imager 600 (GE, USA).

Primary antibodies

The primary antibodies used for immunoblotting (IB) or immunofluorescence (IF) were as follows: anti-HA high affinity (3F10, rat monoclonal IgG, 1:3000 for IB and 1:50 for IF; Roche, Switzerland), anti-α-tubulin (mouse monoclonal IgG, 1:5000 for IB and 1:200 for IF; Proteintech, USA), anti-α-tubulin (rabbit monoclonal IgG, 1:5000 for IB; Proteintech, USA), anti-centrin (clone 20H5, mouse monoclonal IgG, 1:400 for IF; Merck Millipore, Germany), anti-acetylated α-tubulin (clone 6-11B-1, mouse monoclonal IgG, 1:200 for IF; Sigma, USA), anti-CEP290 (rabbit polyclonal IgG, 1:200 for IF; a gift from Dr. George Witman), anti-NPHP4 (rabbit polyclonal IgG, 1:100 for IF; a gift from Dr. George Witman), anti-FMG-1B (#61, mouse monoclonal IgG, 1:100 for IB, Developmental Studies Hybridoma Bank), anti-IFT122 (rabbit polyclonal IgG, 1:2000 for IB and 1:100 for IF), anti-IFT121 (rabbit polyclonal serum, 1:2000 for IB), anti-IFT172 (rabbit polyclonal IgG, 1:2000 for IB), anti-IFT57 (rabbit polyclonal IgG, 1:2000 for IB and 1:100 for IF), anti-IFT54 (rabbit polyclonal serum, 1:2000 for IB), anti-IFT43 (rabbit polyclonal serum, 1:100 for IF), anti-IFT38 (rabbit polyclonal IgG, 1:5000 for IB and 1:100 for IF), anti-FLA10 (rabbit polyclonal IgG, 1:3000 for IB), anti-D1BLIC (rabbit polyclonal IgG, 1:2000 for IB), anti-BBS8 (rabbit polyclonal IgG, 1:250 for IB), anti-RIB72 (rabbit polyclonal IgG, 1:3000 for IB), anti-IC2 (mouse monoclonal IgG, 1:20000 for IB; Sigma, USA), anti-PSAD (rabbit polyclonal serum, 1:1000 for IB, 1:500 for IF; a gift from Dr. Xiaobo Li; Agrisera, Sweden), and anti-PSBC (rabbit polyclonal serum, 1:3000 for IB, 1:500 for IF; a gift from Dr. Xiaobo Li; Agrisera, Sweden). A rabbit anti-TCTN1 antibody was generated against bacterial expressed GST-His-tagged TCTN1 (368–490 amino acids) (Abclonal, China) and was only used at a dilution of 1:500 for IF.

Transmission electron microscopy (TEM)

Negative staining and TEM were carried out as previously described [22, 55]. The samples were imaged on an H-7650B transmission electron microscope (Hitachi Limited, Japan) equipped with a digital V600 camera (ATM Company).

Quantitative proteomics

A total of 150 μg of ciliary proteins from each sample was dissolved in RIPA buffer containing protease inhibitor. The dissolved proteins were precipitated and washed with acetone solution. The concentration of redissolved samples was determined with a bicinchoninic acid protein quantification kit (Fisher Scientific, MA, USA). Then, 100 μg of protein was reduced with 5 mM dithiothreitol and alkylated with 10 mM iodoacetamide in 100 mM HEPES with 1% SDC. Trypsin (1 μg) was used for protein digestion overnight at 37 °C. SDC and salt were removed, and the peptides were dried in a freeze dryer. The peptides, resuspended in 0.1% TFA, were separated using a Reprosil-Pur 120 C18 analytical column (100 μm ID ×15 cm, 1.9 μm, Dr. Maisch) on a nano-UPLC system (EASY-nLC1200). Then, 0.1% formic acid in acetonitrile/water (2:98) was used as mobile phase A, and 0.1% formic acid in acetonitrile/water (80:20) was used as mobile phase B. A Q-Exactive HFX mass spectrometer (Thermo Scientific, MA, USA) was operated in data-dependent acquisition mode for sample analysis. MS1 was performed in a range of 350–1600 *m/z* with a resolution of 120,000 (200 *m/z*). The top 20 precursor ions were fragmented by high-energy C-trap dissociation (HCD) with a normalized collision energy (NCE) of 27%. In MS/MS, the resolution was set to 15,000, the AGC control was 1.0×10^5, the maximum ion introduction time was 110 ms, and the dynamic exclusion time was 45 seconds. The MS/MS spectra from each run were searched against the species-level UniProt FASTA databases (*Chlamydomonas reinhardtii*, 2020-01-11, total entries 31247, reviewed entries 339, unreviewed entries 30908). The raw data were processed using Proteome Discoverer (PD) software. The search criteria were as follows: tryptic digestion, 2 missed cleavages allowed, carbamidomethyl (C) set as a fixed modification, and oxidation (M) and acetyl (protein N-term) set as variable modifications. Peptide identification was carried out with an initial precursor ion mass deviation of up to 10 ppm and a fragment mass deviation of 0.02 Da. For protein identification, the false discovery rate (FDR) was set at 0.01 for both peptide spectral matches (PSMs) and peptide levels. Total peptide was used for normalization, and both unique peptides and razor peptides were used for further quantification. Other parameters were set as default.

Acknowledgments

We thank Dr. George Witman and Dr. Xiaobo Li for kindly providing antibodies. We would also like to thank Dr. Jun Lu and Dr. Yuanlin Zheng for equipment support. We are grateful to the Center of Biomedical Analysis (Tsinghua University, China) for their excellent help with the electron microscopy analysis.

This work was supported by the National Natural Science Foundation of China (91954123, 31972887, and 31972888), the Natural Science Foundation of Jiangsu Province (BK20191465), Clinical Research Projects of Shanghai Municipal Health Commission (20194Y0133), and the Priority Academic Program Development of Jiangsu Higher Education Institutions (PAPD).

Author Contributions

L.W., X.W., and M.C. designed, performed the experiments, and analyzed the data. Z.L., C.L., H.Z., H.Y., Y.L., Y.C., and Z.W. performed the experiments. G.L. analyzed the data. J.P., L.W., and M.C. conceived the idea, analyzed the data and wrote the manuscript. All authors approved the final manuscript.

Competing Interest Statement

The authors declare no competing interests.

Data availability

The data that support the findings of this study are available from the corresponding author upon reasonable request.

References

1. Ishikawa H, Marshall WF. Ciliogenesis: building the cell's antenna. *Nat Rev Mol Cell Biol* **12**, 222-234 (2011).
2. Satir P. CILIA: before and after. *Cilia* **6**, 1 (2017).
3. Bayless BA, Navarro FM, Winey M. Motile Cilia: Innovation and Insight From Ciliate Model Organisms. *Front Cell Dev Biol* **7**, 265 (2019).
4. Lechtreck KF. IFT-Cargo Interactions and Protein Transport in Cilia. *Trends Biochem Sci* **40**, 765-778 (2015).
5. Nachury MV. The molecular machines that traffic signaling receptors into and out of cilia. *Curr Opin Cell Biol* **51**, 124-131 (2018).
6. Takao D, Wang L, Boss A, Verhey KJ. Protein Interaction Analysis Provides a Map of the Spatial and Temporal Organization of the Ciliary Gating Zone. *Curr Biol* **27**, 2296-2306 e2293 (2017).
7. Sreekumar V, Norris DP. Cilia and development. *Curr Opin Genet Dev* **56**, 15-21 (2019).
8. Youn YH, Han YG. Primary Cilia in Brain Development and Diseases. *Am J Pathol* **188**, 11-22 (2018).
9. Garcia-Gonzalo FR, Reiter JF. Open Sesame: How Transition Fibers and the Transition Zone Control Ciliary Composition. *Cold Spring Harb Perspect Biol* **9**, (2017).
10. Mitchison HM, Valente EM. Motile and non-motile cilia in human pathology: from function to phenotypes. *J Pathol* **241**, 294-309 (2017).
11. Anvarian Z, Mykytyn K, Mukhopadhyay S, Pedersen LB, Christensen ST. Cellular signalling by primary cilia in development, organ function and disease. *Nat Rev Nephrol* **15**, 199-219 (2019).
12. Wallmeier J*, et al.* Motile ciliopathies. *Nat Rev Dis Primers* **6**, 77 (2020).
13. Reiter JF, Leroux MR. Genes and molecular pathways underpinning ciliopathies. *Nat Rev Mol Cell Biol* **18**, 533-547 (2017).
14. Johnstone RM, Adam M, Hammond JR, Orr L, Turbide C. Vesicle formation during reticulocyte maturation. Association of plasma membrane activities with released vesicles (exosomes). *J Biol Chem* **262**, 9412-9420 (1987).
15. Heijnen HF, Schiel AE, Fijnheer R, Geuze HJ, Sixma JJ. Activated platelets release two types of membrane vesicles: microvesicles by surface shedding and exosomes derived from exocytosis of multivesicular bodies and alpha-granules. *Blood* **94**, 3791-3799 (1999).
16. Denzer K, Kleijmeer MJ, Heijnen HF, Stoorvogel W, Geuze HJ. Exosome: from internal vesicle of the multivesicular body to intercellular signaling device. *J Cell Sci* **113 Pt 19**, 3365-3374 (2000).

17. Cocucci E, Meldolesi J. Ectosomes and exosomes: shedding the confusion between extracellular vesicles. *Trends Cell Biol* **25**, 364-372 (2015).
18. van Niel G, D'Angelo G, Raposo G. Shedding light on the cell biology of extracellular vesicles. *Nat Rev Mol Cell Biol* **19**, 213-228 (2018).
19. Wood CR, Huang K, Diener DR, Rosenbaum JL. The cilium secretes bioactive ectosomes. *Curr Biol* **23**, 906-911 (2013).
20. Long H*, et al.* Comparative Analysis of Ciliary Membranes and Ectosomes. *Curr Biol* **26**, 3327-3335 (2016).
21. Wood CR, Rosenbaum JL. Ciliary ectosomes: transmissions from the cell's antenna. *Trends Cell Biol* **25**, 276-285 (2015).
22. Cao M*, et al.* Uni-directional ciliary membrane protein trafficking by a cytoplasmic retrograde IFT motor and ciliary ectosome shedding. *Elife* **4**, (2015).
23. Nager AR*, et al.* An Actin Network Dispatches Ciliary GPCRs into Extracellular Vesicles to Modulate Signaling. *Cell* **168**, 252-263 e214 (2017).
24. Phua SC*, et al.* Dynamic Remodeling of Membrane Composition Drives Cell Cycle through Primary Cilia Excision. *Cell* **168**, 264-279 e215 (2017).
25. Luxmi R, Kumar D, Mains RE, King SM, Eipper BA. Cilia-based peptidergic signaling. *PLoS Biol* **17**, e3000566 (2019).
26. Matsuda Y, Saito T, Yamaguchi T, Koseki M, Hayashi K. Topography of cell wall lytic enzyme in Chlamydomonas reinhardtii: form and location of the stored enzyme in vegetative cell and gamete. *J Cell Biol* **104**, 321-329 (1987).
27. Gogendeau D*, et al.* MKS-NPHP module proteins control ciliary shedding at the transition zone. *PLoS Biol* **18**, e3000640 (2020).
28. Shimada H*, et al.* In Vitro Modeling Using Ciliopathy-Patient-Derived Cells Reveals Distinct Cilia Dysfunctions Caused by CEP290 Mutations. *Cell Rep* **20**, 384-396 (2017).
29. Li A*, et al.* Ciliary transition zone activation of phosphorylated Tctex-1 controls ciliary resorption, S-phase entry and fate of neural progenitors. *Nat Cell Biol* **13**, 402-411 (2011).
30. Garcia-Gonzalo FR*, et al.* A transition zone complex regulates mammalian ciliogenesis and ciliary membrane composition. *Nat Genet* **43**, 776-784 (2011).
31. Yee LE*, et al.* Conserved Genetic Interactions between Ciliopathy Complexes Cooperatively Support Ciliogenesis and Ciliary Signaling. *PLoS Genet* **11**, e1005627 (2015).
32. Sanders MA, Salisbury JL. Centrin-mediated microtubule severing during flagellar excision in Chlamydomonas reinhardtii. *J Cell Biol* **108**, 1751-1760 (1989).
33. Craige B*, et al.* CEP290 tethers flagellar transition zone microtubules to the membrane and regulates flagellar protein content. *J Cell Biol* **190**, 927-940 (2010).
34. Pazour GJ, Agrin N, Leszyk J, Witman GB. Proteomic analysis of a eukaryotic cilium. *J Cell Biol* **170**, 103-113 (2005).
35. Diener DR, Lupetti P, Rosenbaum JL. Proteomic analysis of isolated ciliary transition zones reveals the presence of ESCRT proteins. *Curr Biol* **25**, 379-384 (2015).
36. Awata J*, et al.* NPHP4 controls ciliary trafficking of membrane proteins and large soluble proteins at the transition zone. *J Cell Sci* **127**, 4714-4727 (2014).

37. Weng RR, Yang TT, Huang CE, Chang CW, Wang WJ, Liao JC. Super-Resolution Imaging Reveals TCTN2 Depletion-Induced IFT88 Lumen Leakage and Ciliary Weakening. *Biophys J* **115**, 263-275 (2018).
38. Wang C, Li J, Meng Q, Wang B. Three Tctn proteins are functionally conserved in the regulation of neural tube patterning and Gli3 processing but not ciliogenesis and Hedgehog signaling in the mouse. *Dev Biol* **430**, 156-165 (2017).
39. Wang J*, et al.* Sensory cilia act as a specialized venue for regulated extracellular vesicle biogenesis and signaling. *Curr Biol*, (2021).
40. Long H, Huang K. Transport of Ciliary Membrane Proteins. *Front Cell Dev Biol* **7**, 381 (2019).
41. Sang L*, et al.* Mapping the NPHP-JBTS-MKS protein network reveals ciliopathy disease genes and pathways. *Cell* **145**, 513-528 (2011).
42. Li C*, et al.* MKS5 and CEP290 Dependent Assembly Pathway of the Ciliary Transition Zone. *PLoS Biol* **14**, e1002416 (2016).
43. Williams CL*, et al.* MKS and NPHP modules cooperate to establish basal body/transition zone membrane associations and ciliary gate function during ciliogenesis. *J Cell Biol* **192**, 1023-1041 (2011).
44. Chih B*, et al.* A ciliopathy complex at the transition zone protects the cilia as a privileged membrane domain. *Nat Cell Biol* **14**, 61-72 (2012).
45. Wiegering A*, et al.* Cell type-specific regulation of ciliary transition zone assembly in vertebrates. *EMBO J* **37**, (2018).
46. Lambacher NJ*, et al.* TMEM107 recruits ciliopathy proteins to subdomains of the ciliary transition zone and causes Joubert syndrome. *Nat Cell Biol* **18**, 122-131 (2016).
47. Yang TT*, et al.* Superresolution Pattern Recognition Reveals the Architectural Map of the Ciliary Transition Zone. *Sci Rep* **5**, 14096 (2015).
48. Shiba D, Yokoyama T. The ciliary transitional zone and nephrocystins. *Differentiation* **83**, S91-96 (2012).
49. Jensen VL*, et al.* Formation of the transition zone by Mks5/Rpgrip1L establishes a ciliary zone of exclusion (CIZE) that compartmentalises ciliary signalling proteins and controls PIP2 ciliary abundance. *EMBO J* **34**, 2537-2556 (2015).
50. Wang L*, et al.* Rapid and high efficiency transformation of Chlamydomonas reinhardtii by square-wave electroporation. *Biosci Rep* **39**, (2019).
51. Gonzalez-Ballester D, de Montaigu A, Galvan A, Fernandez E. Restriction enzyme site-directed amplification PCR: a tool to identify regions flanking a marker DNA. *Anal Biochem* **340**, 330-335 (2005).
52. Wang L*, et al.* Flagellar regeneration requires cytoplasmic microtubule depolymerization and kinesin-13. *J Cell Sci* **126**, 1531-1540 (2013).
53. Meng D, Pan J. A NIMA-related kinase, CNK4, regulates ciliary stability and length. *Mol Biol Cell* **27**, 838-847 (2016).
54. Lefebvre PA, Nordstrom SA, Moulder JE, Rosenbaum JL. Flagellar elongation and shortening in Chlamydomonas. IV. Effects of flagellar detachment, regeneration, and resorption on the induction of flagellar protein synthesis. *J Cell Biol* **78**, 8-27 (1978).
55. Meng D, Cao M, Oda T, Pan J. The conserved ciliary protein Bug22 controls planar beating of Chlamydomonas flagella. *J Cell Sci* **127**, 281-287 (2014).

Figures

Fig. 1: Characterization of the *C. reinhardtii tctn1* mutant.

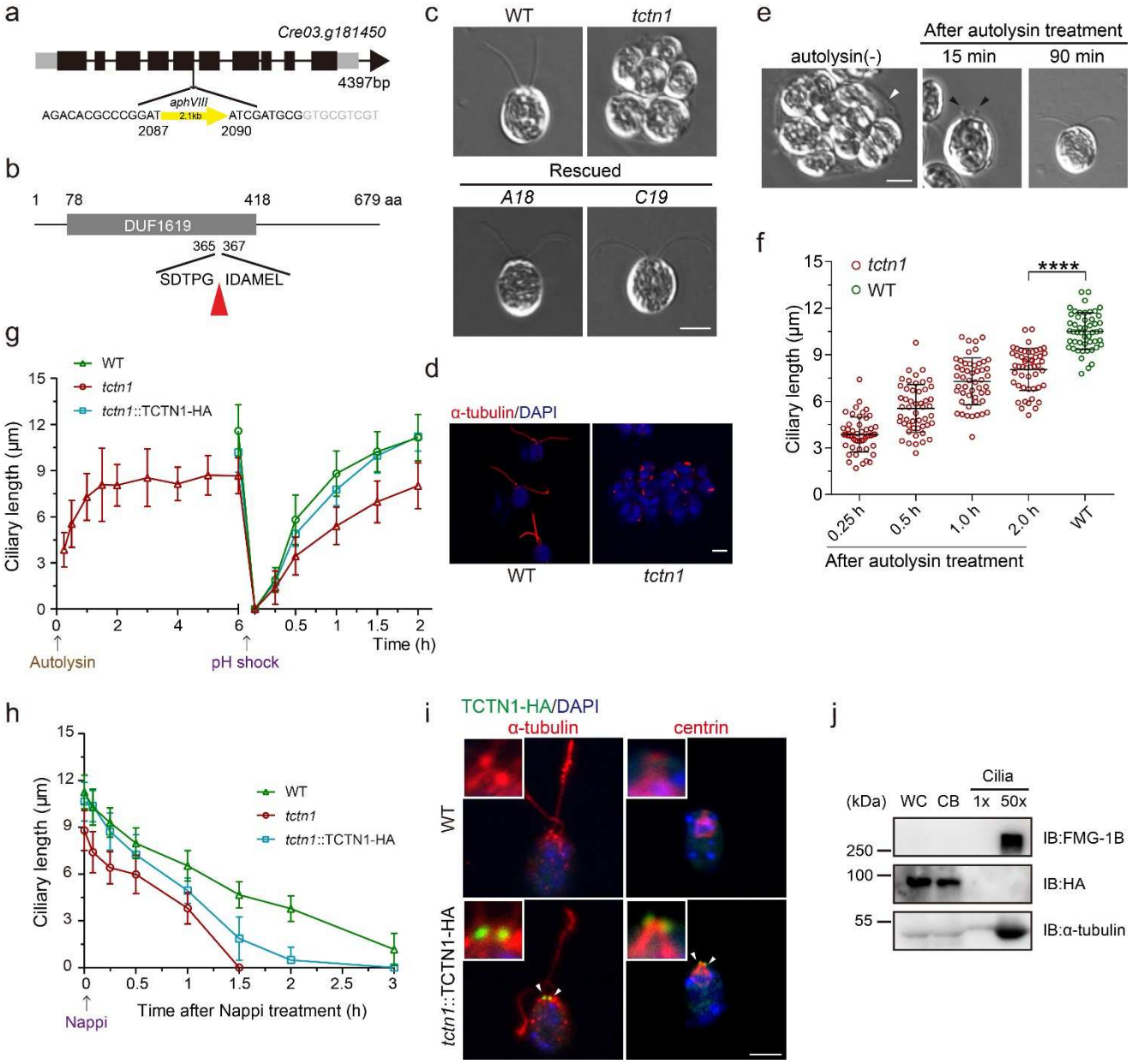

a Diagram of the gene structure of *TCTN1* (*Cre03.g181450*) with the resistance DNA insertional site. The *aphVIII* DNA fragment (~ 2.1 kb) was inserted in the fifth exon of *TCTN1*. The yellow box with the arrow indicates the insertional site. **b** Diagram of the domain structure of the TCTN1 protein. The TCTN1 protein (679 aa) contains the DUF1619 domain (78-418 aa) with unknown function. The red arrowhead marks the insertional site. **c** DIC images showing the ciliary phenotypes of WT, mutant, and rescued cells (*A18*, *C19*). The *tctn1* mutant are palmelloid (cells failed to hatch from the mother cell wall after mitosis). *TCTN1* tagged with 3 × HA at the C-terminus was transformed into *tctn1* to rescue the mutant. Scale bar, 5 μm. **d** Immunostaining images depicting the very short cilium within the palmelloid of *tctn1*. The red signals (by anti-α-tubulin antibody) mark the cilia and the blue signals (by DAPI) mark the nucleus. Scale bar, 5 μm. **e** DIC images depicting the ciliary phenotype of *tctn1* after treatment with autolysin. The *tctn1* cells released from the mother cell walls (white arrowhead) and elongated cilia, and occasionally with the bugles (black arrowheads) at the short ciliary tip. Scale bar, 5 μm. **f** Scatter plot showing the elongation of cilia of

cells hatched from the palmelloid after autolysin treatment. Statistical significance was determined with an unpaired *t* test. ****, P<0.0001. **g** *tctn1* exhibited shorter cilia after hatching with autolysin and slower kinetics of ciliary assembly. The arrow indicates the time point of autolysin treatment to release cells or pH shock treatment for deciliation. **h** *tctn1* exhibited faster kinetics of ciliary disassembly. The arrow indicates the time point of Nappi treatment to induce ciliary shortening. **i** Immunostaining showing the localization of TCTN1 in the TZ. WT and the rescued cells expressing TCTN1-HA were immunostained with HA (green) and α-tubulin (red, left) or centrin (red, right) antibodies. The nucleus was stained with DAPI (blue). The arrowheads indicate the TZ at the ciliary base. The insets show higher magnification views of the TZ region. Scale bar, 5 μm. **j** Immunoblot analysis of the localization of TCTN1-HA in the rescued cell line. Cell body and cilia were isolated from the rescued cells . 1 × (cilia) represents an equal proportion of cilia to that of the cell body (two cilia per cell body). 50 × (cilia) represents equal cilia and cell body proteins. WC, whole cell. CB, cell body. Ciliary lengths are shown as the mean ± SD of 50 cilia and repeated three times in this figure.

Fig. 2: Loss of TCTN1 causes TZ defects similar to those caused by loss of NPHP4 and CEP290.

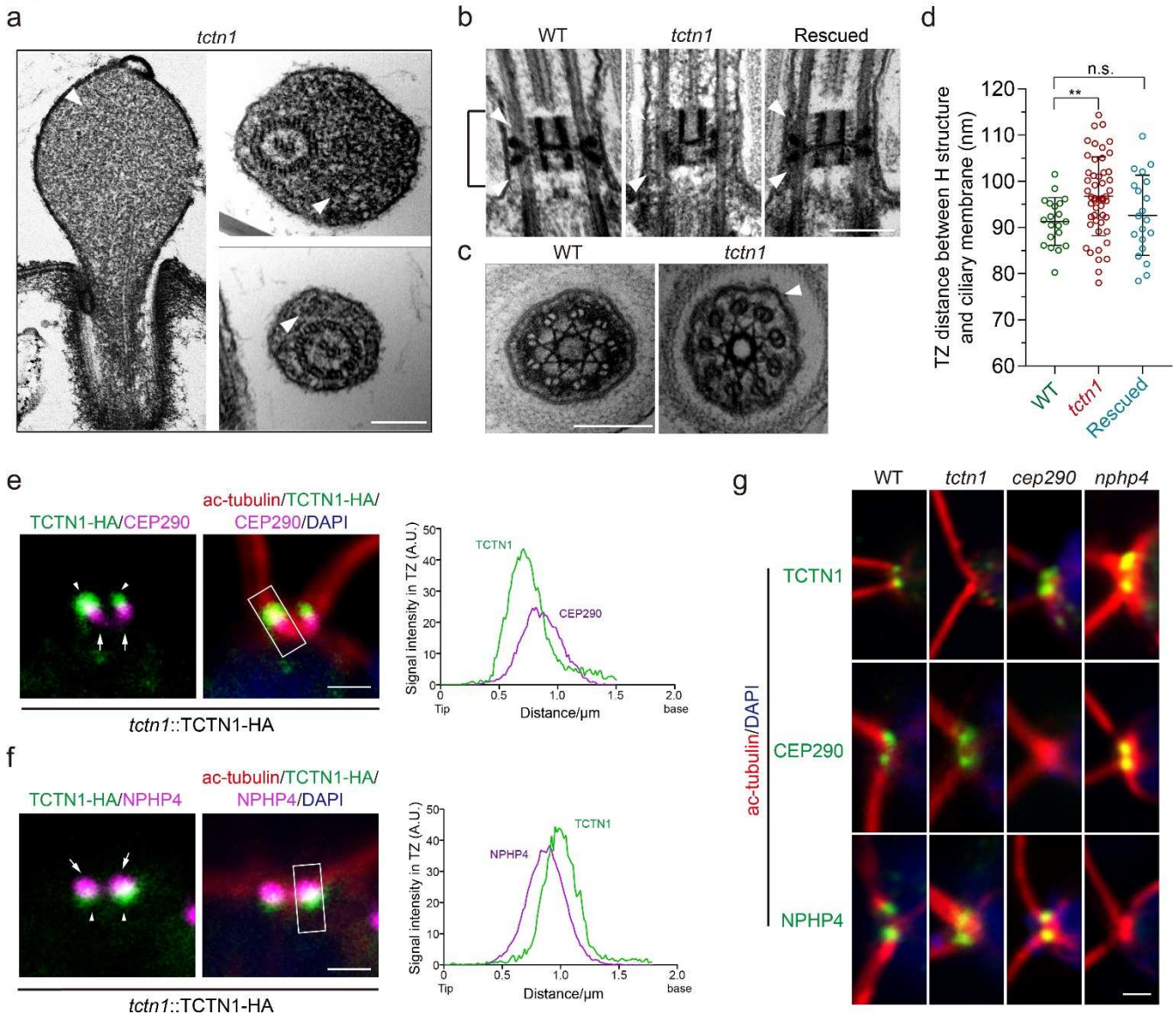

a EM images showing ciliary bulges with electron-dense material (white arrowheads) in a portion of *tctn1* cells. Scale bar, 200 nm. **b, c** Longitudinal sections and cross sections through the TZ (brackets) of WT, *tctn1* and rescued cells. Y-links (white arrowheads) between the TZ microtubules and ciliary membrane were present in WT and rescued cells but were missing in *tctn1* cells. Scale bar, 200 nm. **d** Scatter plot depicting the distances between the H structure and the ciliary membrane in WT, *tctn1*, and rescued cells. Data are the mean ± SD (n=20). Statistical significance was determined with an unpaired *t* test. n.s., not significant. **, P<0.01. **e, f** Immunostaining images and graphs depicting the colocalization of TCTN1 and NPHP4/CEP290. The rescued cells expressing TCTN1-HA were immunostained with anti-acetylated α-tubulin (ac-tubulin, red), anti-HA (green) and anti-CEP290 (**e**, magenta) or anti-NPHP4 (**f**, magenta) antibodies. The nucleus was stained with DAPI (blue). The arrowheads and arrows indicate the localization of TCTN1-HA and CEP290/NPHP4, respectively. The scan plots of the rectangular gray value in the merged image show the relative intensities (A.U.) of the indicated proteins in the TZ. Scale bar, 1 μm. **g** Immunostaining depicting the TZ localization of TCTN1, NPHP4, and CEP290 in WT, *tctn1*, *cep290*, and *nphp4* cells. Cells as indicated were immunostained with anti-acetylated α-tubulin (ac-tubulin, red), anti-TCTN1/ CEP290/NPHP4 (green) antibodies. The nucleus was stained with DAPI (blue). Scale bar, 1 μm.

Fig. 3: The integrity of TCTN1 is essential for its ciliary function.

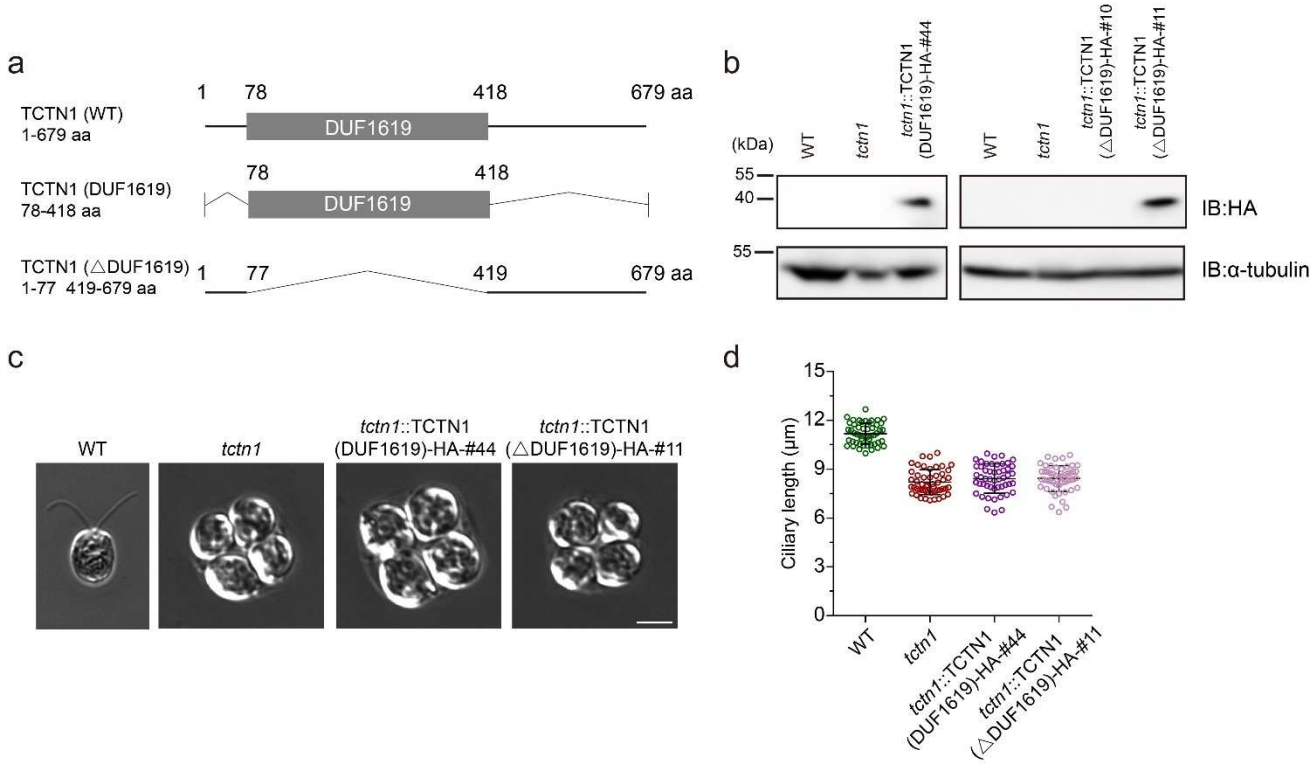

a Diagram of the domain structure and truncated mutants of TCTN1. The TCTN1 (DUF1619) protein contains the region of 78-418 aa of TCTN1, while the TCTN1 (△DUF1619) protein contains the region of 1-77 aa and 419-679 aa of TCTN1. **b** Immunoblot analysis of the expression of truncated versions of TCTN1, denoted TCTN1 (DUF1619)-HA and TCTN1 (△DUF1619)-HA. Cell lysates from the indicated cells were subjected to immunoblotting and probed with the indicated antibodies. WT and *tctn1* cells were used as negative controls. α-tubulin was used as a loading control. The positions of standard proteins and their molecular masses in kDa are indicated. **c** DIC images showing the ciliary phenotypes of WT, *tctn1*, and *tctn1* mutant cells expressing truncated TCTN1. Both *tctn1* and the truncated TCTN1 expressing cell lines showed palmelloid form, suggesting the truncated TCTN1 could not rescue the phenotype of *tctn1* mutant. Scale bar, 5 μm. **d** Scatter plot depicting the mean ± SD (n=50) of ciliary length of WT, *tctn1*, and cells expressing the truncated versions of TCTN1.

Fig. 4: Loss of TCTN1 attenuates the ciliary gating role of the TZ.

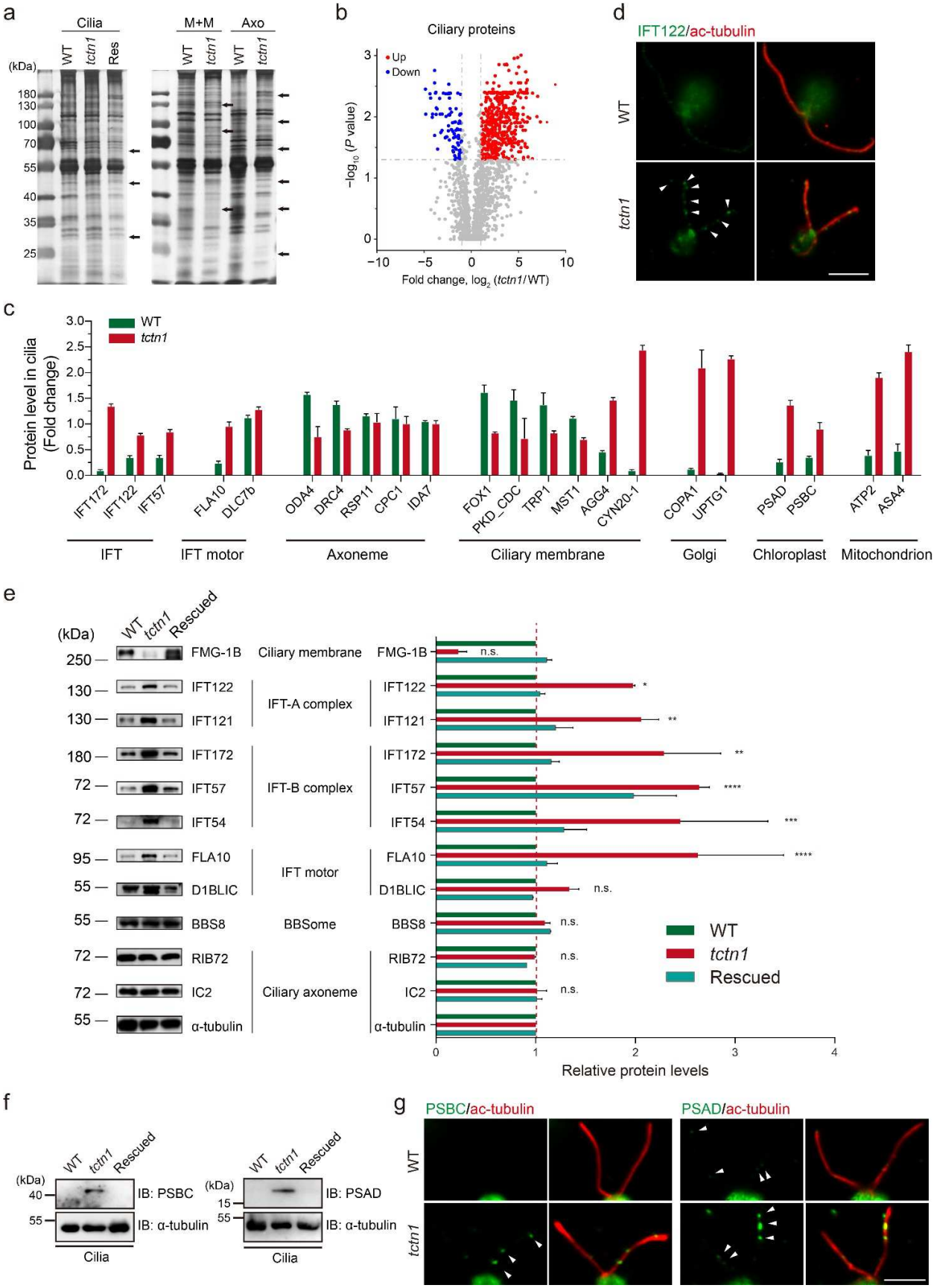

a SDS–PAGE and silver staining of isolated whole cilia or fractionations of cilia from WT, *tctn1*, and rescued cells expressing TCTN1-HA. The samples as indicated were separated on 10% SDS-PAGE and then visualized by silver staining to observe the differences of the protein composition from WT, *tctn1*, and rescued cells. The positions of standard proteins and their molecular masses in kDa are indicated. Arrows indicate the differences among samples. Res, rescued cells. Cilia, ciliary samples. M+M, membrane and matrix samples of cilia. Axo, axonemal samples of cilia. **b** Volcano plot displaying the differentially expressed proteins in cilia between the WT and *tctn1* mutant. The X axis corresponds to the $\log_2$-fold change value of *tctn1*/WT, while the Y axis corresponds to statistical significance in terms of the $-\log_{10}$ (P value). The red and blue dots represent the upregulated and downregulated proteins in cilia of the *tctn1* mutant. **c** Column graph depicting the fold changes in the representative proteins in cilia between WT and *tctn1*. The representative proteins were selected from the mass spectrometry data in **b** and grouped into IFT, IFT motor, axoneme, ciliary membrane, Golgi, chloroplast, and mitochondrion proteins. **d** Immunostaining images displaying the enrichment of IFT122 particles in the cilium of *tctn1*. WT and *tctn1* cells were immunostained with anti-IFT122 (green) and anti-acetylated α-tubulin (ac-tubulin, red) antibodies. The arrowheads indicate the accumulations of IFT122 in the cilium. Scale bar, 5 μm. **e** Immunoblot and statistical analysis of the isolated cilia from WT, *tctn1*, and rescued cells. The ciliary membrane protein (FMG-1B) was downregulated in cilia, while IFT-A complex (IFT121 and IFT122), IFT-B complex (IFT54, IFT57, and IFT172), and IFT motor (FLA10 and D1BLIC) proteins were accumulated in *tctn1* cilia, and the BBSome (BBS8) and ciliary axonemal protein (RIB72 and IC2) levels were comparable with those in WT. α-tubulin was used as a loading control. The positions of standard proteins and their molecular masses in kDa are indicated. The graph showing the gray value of the immunoreactive bands was prepared using the mean ± SEM (n=2). Statistical significance to WT group was determined using two-way ANOVA. n.s., not significant. *, P<0.1. **, P<0.01. ***, P<0.001. ****, P<0.0001. **f** Immunoblot of cilia isolated from WT, *tctn1*, and rescued cells. The antibodies against photosystem proteins (PSBC and PSAD) were used for the confirmation of proteomics results from **b**. The positions of standard proteins and their molecular masses in kDa are indicated. **g** Immunostaining images showing enrichment of photosystem proteins (PSBC, PSAD) in *tctn1*. WT and *tctn1* cells were immunostained with anti-PSBC (green, left), or anti-PSAD (green, right) and anti-acetylated α-tubulin (ac-tubulin, red) antibodies. The non-ciliary proteins were transported and accumulated within the cilium. The arrowheads indicate the accumulation of photosystem proteins in the cilium. Scale bar, 5 μm.

Fig. 5: Proteins differentially regulated in cilia by different TZ proteins.

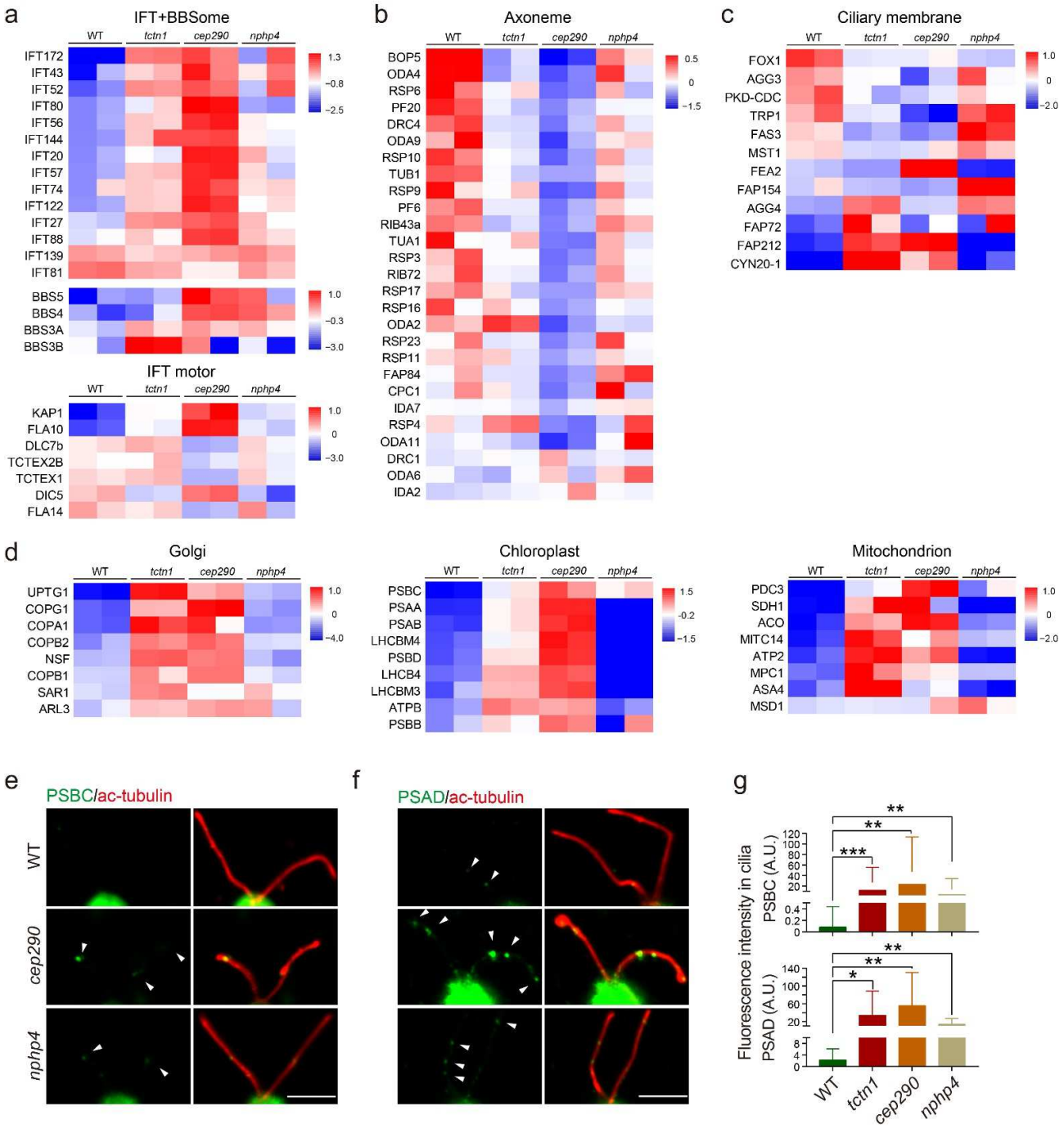

a-d Heatmap of representative groups of proteins identified from ciliary proteomics analysis of cilia from WT, *tctn1*, *cep290*, and *nphp4* cells (two replicates for each strain, column). Representative proteins were selected from the mass spectrometry data in Fig. S6*A* and grouped into IFT and BBSome (**a**, top), IFT motor (**a**, bottom), Axoneme (**b**), Ciliary membrane (**c**), Golgi (**d**, left), Chloroplast (**d**, middle) and Mitochondrion (**d**, right) proteins. **e, f** Immunostaining images displaying the enrichment of photosystem proteins (PSBC and PSAD) in TZ mutants (*cep290* and *nphp4*). WT and TZ mutants were immunostained with anti-PSBC (**e**, green), or anti-PSAD (**f**, green) and anti-acetylated α-tubulin (ac-tubulin, red) antibodies. The non-ciliary proteins were transported and accumulated in cilia of TZ mutant cells. The arrowheads indicate the accumulations of photosystem proteins in the

674 cilium. Scale bar, 5 μm. **g** Column graphs show the ciliary fluorescence intensity of PSBC or PSAD. Data are the
675 mean ± SD (n=20). Statistical significance was determined with an unpaired *t* test. *, P<0.1. **, P<0.01. ***, P<0.001.
676

Fig. 6: The formation of ciliary ectosomes is regulated by the integrity of the TZ during gamete mating events.

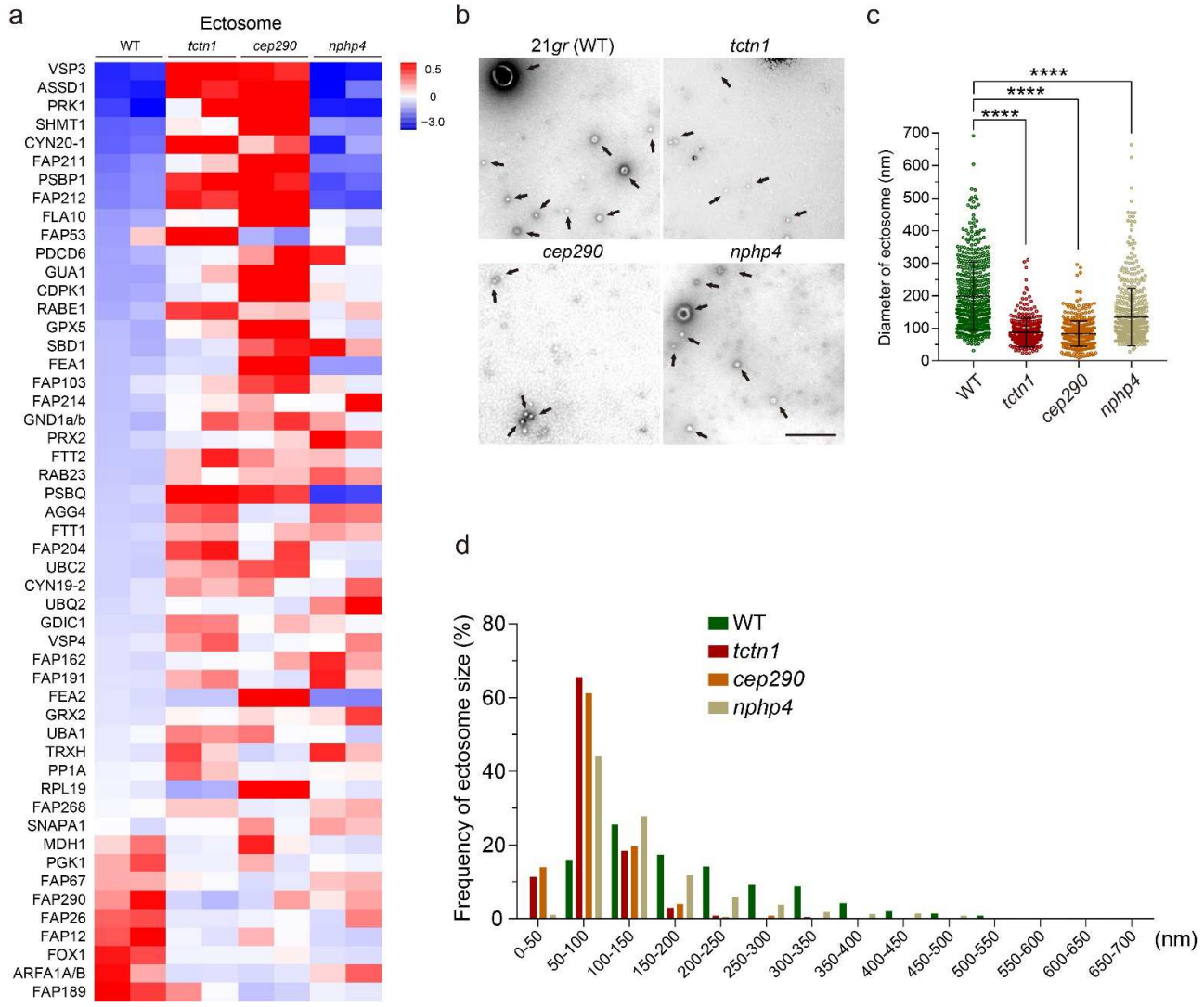

a Heatmap of representative ectosome related proteins identified from ciliary proteomics analysis of cilia from WT, *tctn1*, *cep290*, and *nphp4* cells (two replicates for each strain, column). Representative proteins were selected from the mass spectrometry data in Fig. S6*A*. **b** Negative stain transmission electron micrographs of purified ciliary ectosomes (black arrows) from gametes in the mating process. 21*gr* (WT), ectosomes from mating supernatant of 21*gr* × 6145c; *tctn1*, ectosomes from mating supernatant of *tctn1* × 6145c; *cep290*, ectosomes from mating supernatant of *cep290* × 6145c; *nphp4*, ectosomes from mating supernatant of *nphp4* × 6145c. Scale bar, 500 nm. **c** Scatter plot showing the diameters of ectosomes shedded from the cilia of different mating gametes. The sizes of the ectosomes (n=500) described in **b**. **d** Graph showing the distribution of ciliary ectosomes of different sizes purified from 21*gr* × 6145c, *tctn1* × 6145c, *cep290* × 6145c, and *nphp4* × 6145 described in **b**.

Fig. 7: The activity and protein composition of ciliary ectosomes shedding from gametes of different TZ mutants are different.

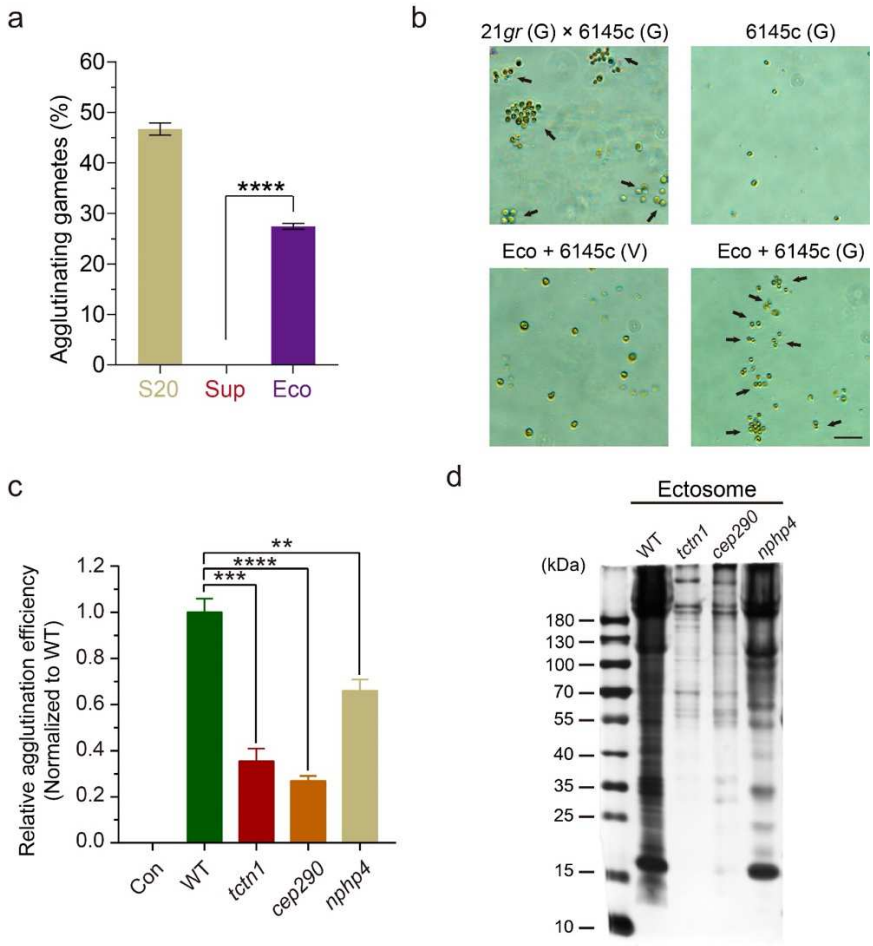

a Column graph depicting the agglutinating gametes number (%) from 6145c (mt-) mixed with the supernatant (S20), the final supernatant (Sup) and ectosome pellet (Eco) from gamete mating culture (21*gr* × 6145c). Data are shown as the mean ± SD (n=3). Statistical significance was determined with an unpaired *t* test. ****, P<0.0001. **b** PH images showing the agglutination of gametic 6145c (mt-) induced by mixing with the ectosomes (Eco). Gametic 6145c alone, vegetative 6145c with Eco, and 21*gr* × 6145c were showed as the negative and positive controls respectively. The black arrows indicate the agglutination of gametic cells. G, gametic cells. V, vegetative cells. Scale bar, 20 μm. **c** Column graph displaying the agglutination efficiency (normalized to WT) of gametic 6145c (mt-) mixed with the ectosome pellet (Eco) from gamete mating cultures (21*gr* × 6145c, *tctn1* × 6145c, *cep290* × 6145c, *nphp4* × 6145c). The group of vegetative 6145c with Eco was as the negative control (Con). **d** Silver-stained SDS–PAGE gel showing protein variations in ectosomes isolated from the plus mating type gamete (21*gr*, *tctn1*, *cep290*, *nphp4*) with minus mating type gamete (6145c). The indicated ciliary ectosomes purified from the same amount of cells were separated on 4% ~ 20% SDS-PAGE and then stained with silver staining to visualize the different amounts and compositions of proteins in different ectosomes. The positions of standard proteins and their molecular masses in kDa are indicated. Data are presented as the mean ± SD in this figure. Statistical significance was determined with an unpaired *t* test. **, P<0.01. ***, P<0.001. ****, P<0.0001.

Supplementary Figure 1. TCTN1 is localized at the TZ.

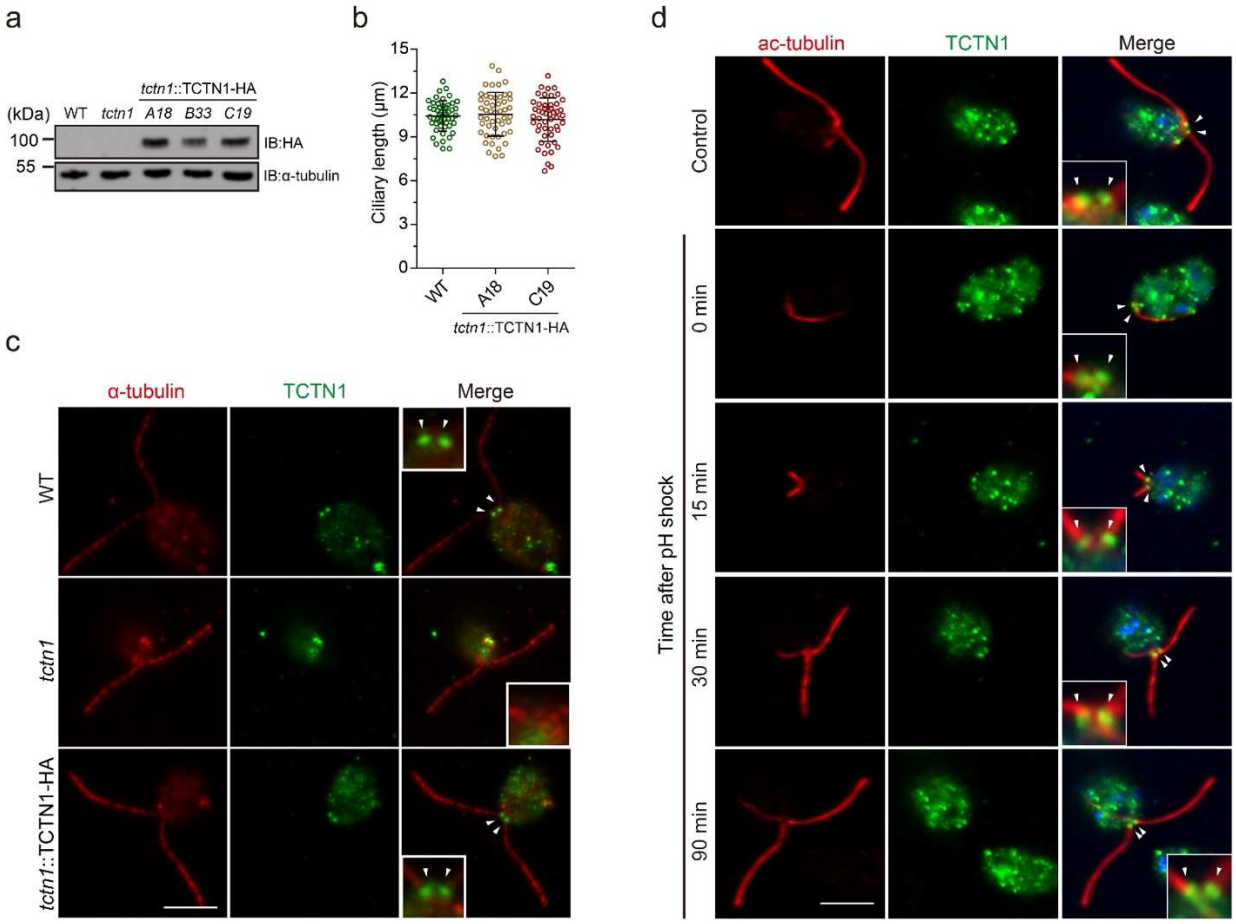

a Immunoblot analysis of the expression of TCTN1-HA in the WT, *tctn1*, and rescued cells. Cell lysates from the indicated cells were subjected to immunoblotting probed with the indicated antibodies. WT and *tctn1* cells were used as negative controls. α-tubulin was used as a loading control. The positions of standard proteins and their molecular masses in kDa are indicated. **b** Scatter plot showing the mean ± SD of ciliary length (n=50) in the WT, *tctn1*, and rescued cells (*A18* and *C19*). **c** Immunostaining images depicting the immunospecificity of the anti-TCTN1 antibody and localization of TCTN1 in the TZ. WT, *tctn1*, and the rescued cells expressing TCTN1-HA were immunostained with anti-TCTN1 (green) and anti-α-tubulin (red) antibodies. The arrowheads indicate the TZ at the ciliary base. The insets show the higher magnification views of the TZ region in the merge image. Scale bar, 5 μm. **d** Immunostaining images illustrating that the localization of TCTN1 in the TZ was not changed during ciliary regeneration. Cells were subjected to pH shock to induce deciliation and collected for immunostaining with anti-TCTN1 (green) and anti-acetylated α-tubulin (ac-tubulin, red) antibodies at the indicated time point. The nucleus was stained with DAPI (blue). The arrowheads indicate the TZ at the ciliary base. The insets show higher magnification views of the TZ region in the merged image. Scale bar, 5 μm.

Supplementary Figure 2. The ciliary phenotypes of *tctn1*, *cep290*, and *nphp4* are different.

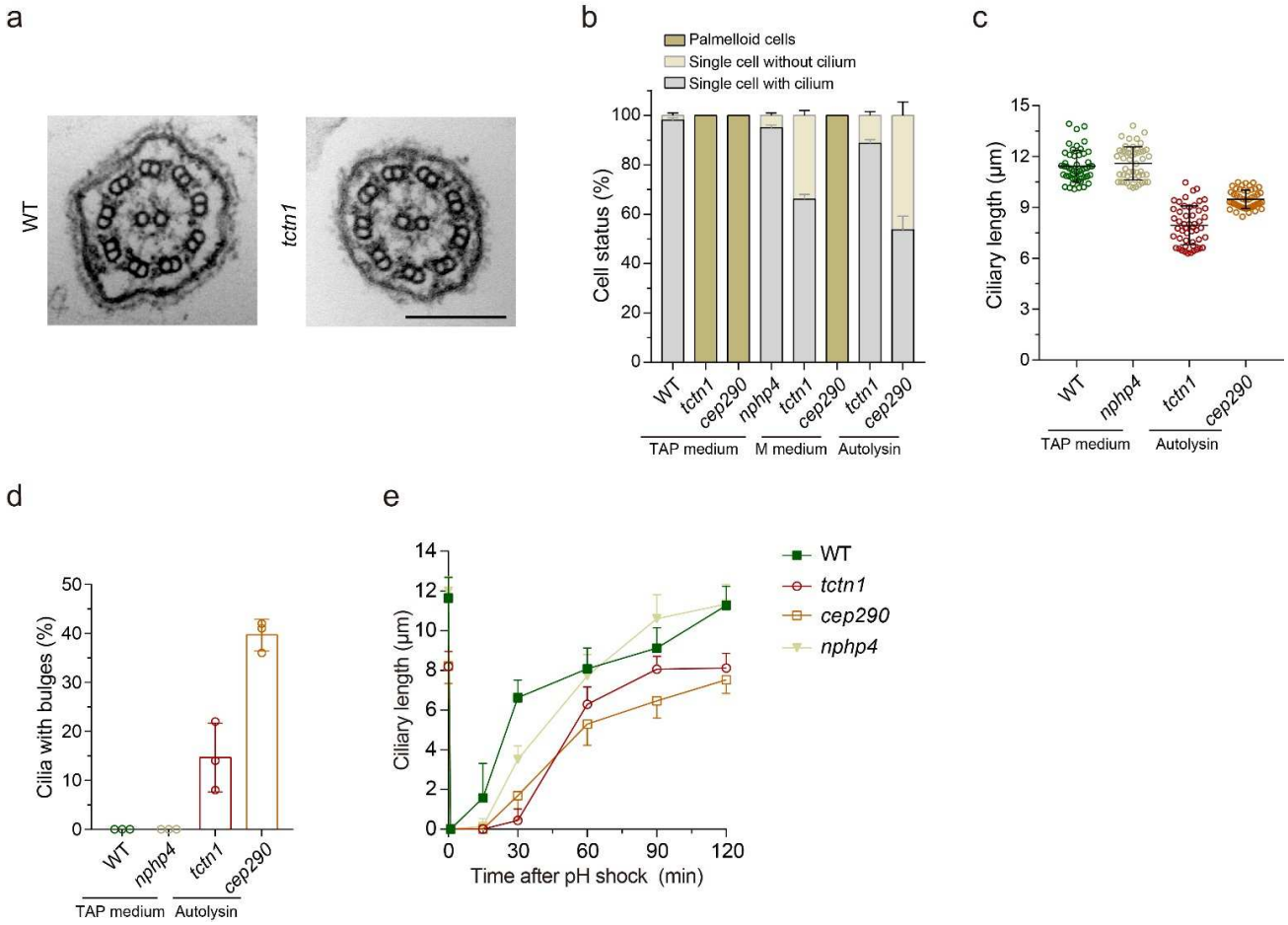

a TEM images showing cross sections through the cilia of WT and *tctn1* cells. Scale bar, 200 nm. **b** Column graph showing the cell status (%) under different conditions (TAP medium, M medium, or after autolysin treatment) for WT, *tctn1*, *cep290*, and *nphp4* cells. **c** Scatter plot showing the average ciliary length under different conditions (TAP medium or after autolysin treatment) for WT, *tctn1*, *cep290*, and *nphp4* cells. **d** Column graph summarizing the percentages of cilia with bulges (%) in WT, *tctn1*, *cep290*, and *nphp4* cells. The palmelloid cells (*tctn1* and *cep290*) were treated with autolysin for hatching before bulge counting. **e** Ciliary regeneration after deciliation by pH shock of WT, *tctn1*, *cep290*, and *nphp4* cells. The palmelloid cells (*tctn1* and *cep290*) were treated with autolysin and grown for 3 h before the deciliation assay and ciliary length analysis. Data are shown as the mean ± SD (n=50 for the ciliary length; n=200 for the cell numbers) in this figure.

743 Supplementary Figure 3. TCTN1 integrity is required for ciliary assembly.

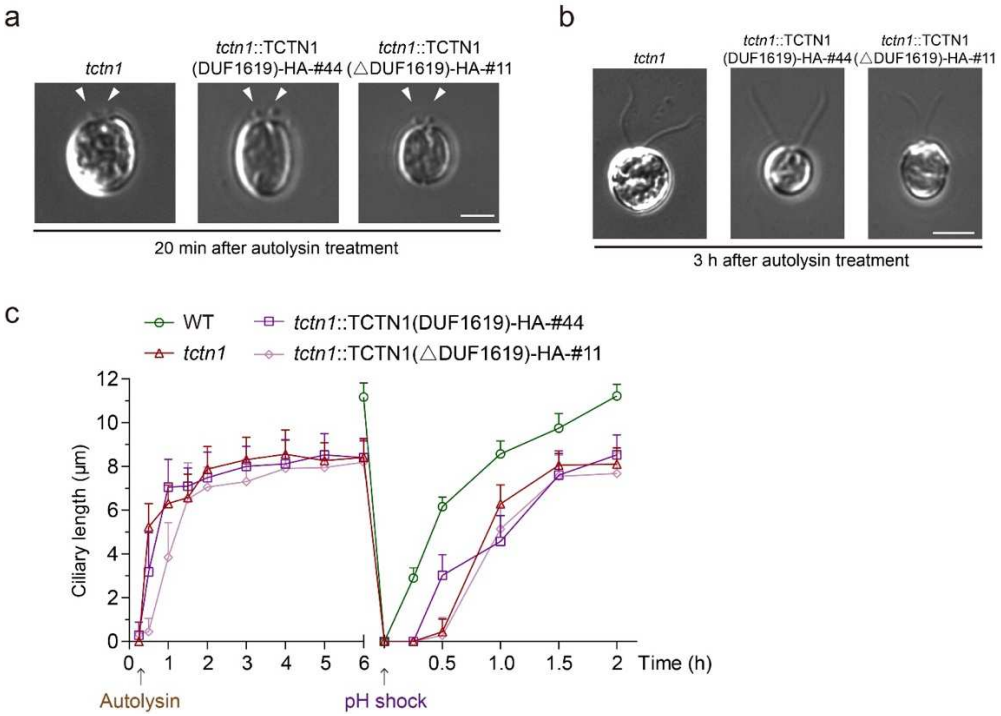

744
745
746 **a** DIC images showing the bulges at the tips of cilia in *tctn1* and in cells expressing the truncated versions of TCTN1.
747 Both *tctn1* and cells expressing truncated TCTN1 hatched after autolysin treatment and showed bulges at the ciliary
748 tips. Scale bar, 5 μm. **b** DIC images showing the elongated cilia in *tctn1* and cells expressing truncated versions of
749 TCTN1 hatched with autolysin. Scale bar, 5 μm. **c** The *tctn1* cells and the cells expressing truncated versions of
750 TCTN1 exhibited shorter cilia after treatment with autolysin and slower kinetics of ciliary assembly. The arrow
751 indicates the time point of autolysin treatment to release cells or pH shock treatment for deciliation. Ciliary length is
752 presented as the mean ± SD (n=50).
753

Supplementary Figure 4. Enrichment of IFT particles in the *tctn1* mutant.

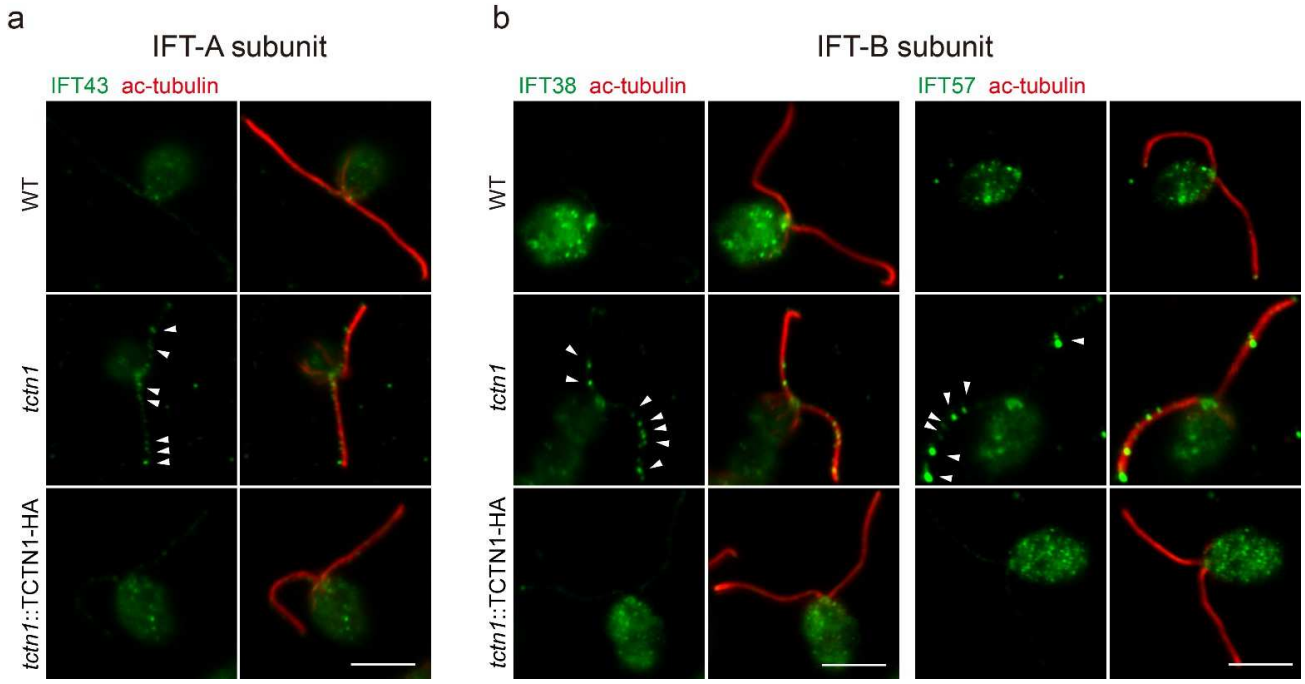

a, b Immunostaining images displaying the enrichment of IFT subunits in *tctn1* cells. WT, *tctn1*, and rescued cells were immunostained with anti-IFT43 (**a**, green), or anti-IFT38 (**b**, left, green), or anti-IFT57 (**b**, right, green), and anti-acetylated α-tubulin (ac-tubulin, red) antibodies. The arrowheads indicate the accumulation of IFT particles in the cilium. Scale bar, 5 μm.

Supplementary Figure 5. PSBC and PSAD staining reveal cup-shaped chloroplasts.

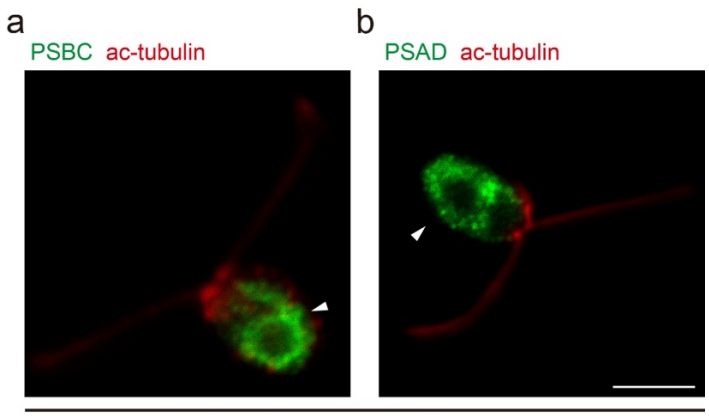

a, b Immunofluorescence images demonstrating the validity of antibodies against the photosystem proteins PSBC and PSAD in the chloroplast of WT cells. WT cells were immunostained with anti-PSBC (**a**, green), or anti-PSAD (**b**, green), and anti-acetylated α-tubulin (ac-tubulin, red) antibodies. The arrowheads show the cup-shaped chloroplasts. Scale bar, 5 μm.

Supplementary Figure 6. The misregulated proteins in different TZ mutants (*tctn1*, *cep290*, and *nphp4*).

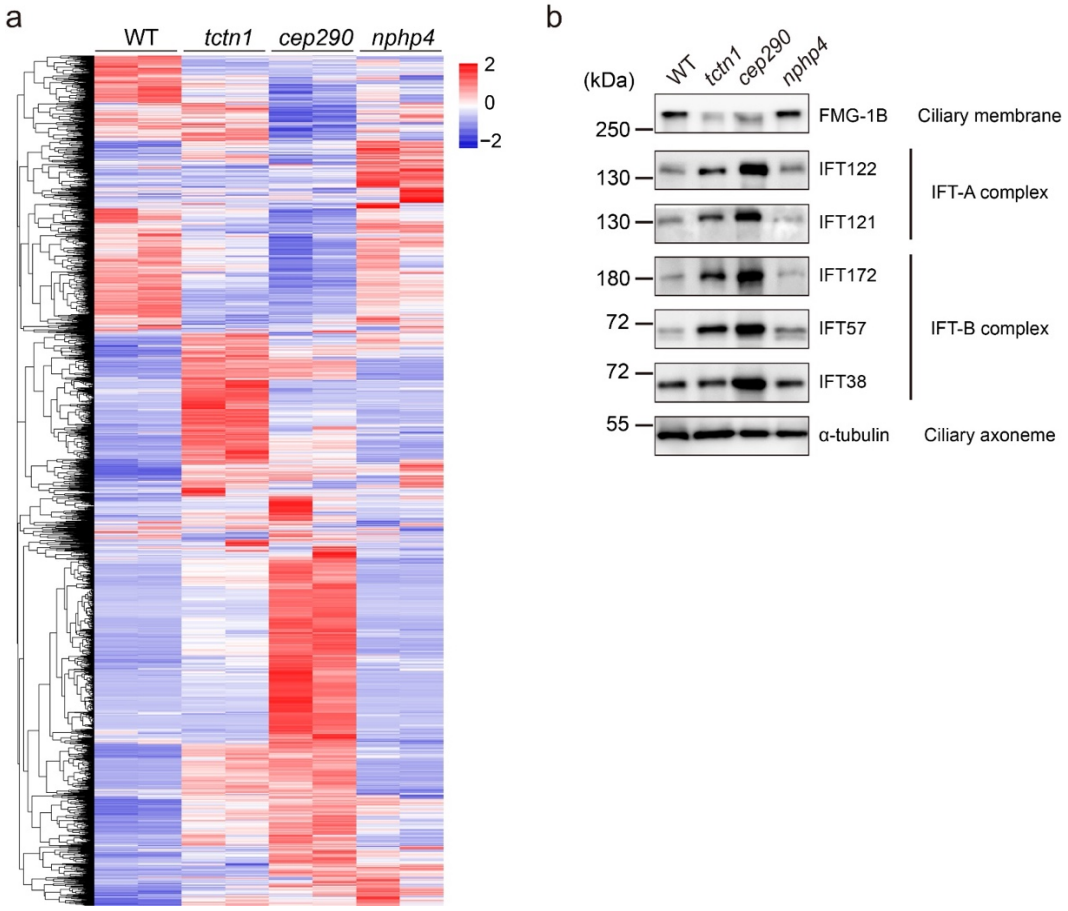

a Heatmap of all 2845 proteins identified in cilia from WT, *tctn1*, *cep290*, and *nphp4*. Fold changes in the expression of proteins from two biological replicates of these four strains are $\log_2$ transformed and displayed as colors ranging from red (upregulated) to blue (downregulated). **b** Immunoblot of cilia isolated from WT, *tctn1*, *cep290*, and *nphp4* cells. Antibodies against FMG1-B, IFT-A complex (IFT121 and IFT122), and IFT-B complex (IFT38, IFT57, and IFT172) were used to confirm the proteomics results shown in A. α-tubulin was used as a loading control. The positions of standard proteins and their molecular masses in kDa are indicated.